Study of Exotic Higgs Decay at Electron-Hadron Colliders

by Michael O'Keefe

Study of Exotic Higgs Decay at Electron-Hadron Colliders

Michael O'Keefe

200967351

A Thesis submitted in partial fulfilment of the requirements for the degree of

Master of Physics

Under the supervision of Dr. Uta Klein

At the

University of Liverpool, Department of Physics

May 2017

Declaration

I confirm that I have not committed plagiarism nor fabricated data when compiling the following piece of work.

Signed: .....

Abstract

This study focuses on exotic Higgs decays at electron-hadron colliders, investigating the full analysis chain and the prospect of obtaining a measurement of this exotic signal. The exotic decay in question is Higgs, produced by charged current vector boson (W^+W^-) fusion, to a pair of supersymmetric scalars predicted by the Next to Minimal Supersymmetric Model (NMSSM). The characteristic signal of the process is 4b's and a forward jet, with some missing energy, i.e. $eq \to \nu_e h q' \to \nu_e \phi\phi q' \to \nu_e b\bar{b}b\bar{b}q'$; resulting from the fact that the scalar couples strongly to the b quark. This is an example of a charged current deep inelastic scattering process, of the electron off one of the constituent quarks in the proton. The branching fractions of the Higgs into the new scalar, and of the scalar into a $b\bar{b}$ pair were set to Br($h \to \phi\phi$)=10% and Br($\phi \to b\bar{b}$)=100% respectively in this study.

Electron-hadron colliders offer a unique place to study such a decay as the decay environment is much cleaner compared to a hadron-hadron collider. This is a detector level study to determine the feasibility of such a measurement by constraining the signal cross section for various scalar mass assumptions and comparing to the dominant charged current multijet backgrounds. In this way, the prospect of obtaining a measurement, and hence detecting a new, supersymmetric particle will be ascertained.

It was found at the Future Circular Collider, which has a centre of mass energy of 3.5 TeV and a luminosity of 100 fb^{-1} per year, that visible cross sections of 1.30 ± 0.13 fb and 1.68 ± 0.16 fb were obtained for scalar masses of 20 and 60 GeV respectively (in 1 year running). These cross sections were obtained using multivariate analysis techniques, namely the use of boosted decision trees, and had significances of 14 and 14.9 respectively. It was also found that with 1 ab^{-1} (10 years running FCC), the 5σ discovery limit was at around Br($h \to \phi\phi$)=1%, with cross sections of 0.13 ± 0.03 and 0.17 ± 0.03, and significances of 5.54 and 5.71 respectively for the 20 and 60 GeV scalars. These results offer exciting prospects for measuring such a decay signal at future collider options, with the multivariate analysis techniques providing excellent signal to background ratios for different scalar mass assumptions.

Contents

1 Introduction

1.1 Theoretical Motivation

Exotic Higgs decays are well motivated in many BSM (beyond Standard Model) theories, such as the Next to Minimal Supersymmetric Model (NMSSM). The NMSSM predicts that each SM fermion has a bosonic superpartner, and that every SM boson has a fermionic superpartner, with the final addidition of a single new scalar boson [1]. A scalar is a particle with zero spin, of which the only measured example is the Higgs itself [2].

The NMSSM is an extension of the Minimal Supersymmetric Model (MSSM) which only predicts the superparticle pairs, without the addition of a new scalar [3]. Supersymmetry itself aims to solve some of the outstanding issues faced by the Standard Model. Examples of these problems include: matter-antimatter asymmetry, what actually is dark matter and also the hierarchy problem. The hierarchy problem is concerned with the fact that gravity is so much weaker than the 3 other fundamental forces, around 10^{24} times weaker than the weak force, which is the second weakest force, and there is no explanation in the standard model as to why this is the case [4].

Another way to pose the question of the hierarchy problem is the fact that the Higgs mass is so much smaller than other energy scales. The scale of gravity is given by the Plank mass, $M_{Planck} = 1/\sqrt{G_N} \approx 1.2 \times 10^{19}$ GeV, which is many orders of magnitude larger than the Higss mass (125 GeV). Supersymmetry solves the heirarchy problem by cancelling some of the divergences that arise as you get closer and closer to the cutoff (Planck) scale [5].

The reason for the inclusion of an additional scalar in the NMSSM is to solve the μ-problem faced by the MSSM. Th μ-problem is similar in nature to the hierarchy problem, namely that the value of μ, which is the supersymmetric mass parameter that gives mass to the Higgsinos (fermionic Higgs superpartners), must be of the order of the electroweak scale. The electroweak scale (246 GeV) is much much smaller than the Planck scale ($\sim 10^{28} eV$), which is the usual cutoff scale for SM renormalizability [6]. Renormalizability is used to get rid of some of the infinities that may arise when considering particles self interactions. An example of renormalization is that electrons can produce a cloud of photons, that in turn can pair produce more electron-positron pairs. This effects the observed mass and the charge of the electron so they are no longer the same as the expected value. To correct this, the theory is changed such that the initial value of the mass and charge are different so the final state values are equal to the expected values.

Also, the scale of μ is very similar to that of supersymmetric symmetry breaking. This is the process where we obtain normal, non supersymmetric physics, from our supersymmetric theory, which is clearly needed to bridge the gap between SUSY theory and experiment [7]. So, the question arises, why are these 2 scales so close to one another, and also so much smaller than the cut off scale?

The inclusion off an additional scalar singlet means that there is an additional singlet superfield S. Superfields are the SUSY equivalent of SM fields in quantum field theory while a singlet again means a system with overall spin zero. As long as S remains massless in the supersymmetric theory, it acquires a vacuum expectation value of the order of the SUSY breaking scale, giving rise to μ of the correct order [8]. In this way, the μ-term is generated via the theory itself, as opposed to in the MSSM where it is included afterwards 'by hand'. This helps alleviate the issue of naturalness of the values faced by MSSM.

1.2 Experimental Motivation

The main motivation for studying this rare decay process at an ep collider is the cleaner decay environment afforded, compared to pp colliders. This is due to the fact that in a pp collision, both protons are made up of quarks with different parton distribution functions, leading to many different final energy states. In an electron-positron collider, the particles can be collided at an exact centre of mass energy, whereas in a pp collider the energies are described by the parton distribution functions. This is a result of not knowing the exact energies of the constituent quarks, so you cannot know the exact centre of mass energy of each colliding pair of particles (quarks). However proton colliders are often used to go to higher energy scales, as electrons are limited by synchrotron radiation. In an ep collider, the high energy of a hadron collider can be added to the precision of an electron collider. A fuller description of this process will be given in Section 1.3, as will the merits of ep colliders be further examined in Section 2.1.

1.3 Exotic Higgs Decay Into Light Scalars

Scattering processes that are mediated by the exchange of a W boson are known as charged current (CC) processes, while processes mediated by the exchange of a Z boson are known as neutral current (NC). The CC process is expected to be the dominant one, with the NC cross sections orders of magnitudes smaller. This is the avenue that will therefore be explored in searching for the new scalar. In studying this process, the background processes must also be understood, as there are many processes with the same final states as the one that will be used to search for ϕ (the NMSSM scalar). These backgrounds must therefore be quantified accordingly. The main channel that will be searched is the $4b$ channel, with the decay process as follows,

$$eq \to \nu_e h q' \to \nu_e \phi\phi q' \to \nu_e b\bar{b}b\bar{b}q'.$$

An example of the decay process can be seen in the Feynmann diagram in Figure 1.

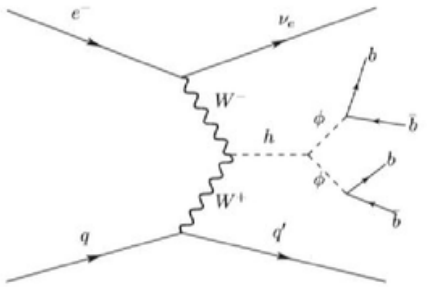

Figure 1: This diagram shows just one of the possible processes that give the correct final state, through the decay of the new NMSSM scalar ϕ. There are many other processes that give this same final state, both signal (ϕ decays) and backgrounds.

The final state in question is 4b plus a forward jet. There will be some missing energy, due to the neutrino, which may also need to be constrained. Another consideration is jet misidentification, or mistagging. Due to colour confinement, bare quarks cannot exist, only colourless combinations can exist stably [9]. Therefore when a quark is created or scattered, the process of hadronisation occurs. The energy of the quark produces other quarks, which then pair off into colourless hadron combinations [10]. In this way, there are no coloured particles overall. This means that the quarks themselves, b quarks in this case, cannot be detected directly, but must be inferred from the jet. This is why b-tagging must be utilised to identify jets resulting from a b quark. b-tagging is simply the identification of jets originating from a b-quark, i.e. flavour tagging. It is therefore possible that a jet not originating from a b-quark may be incorrectly identified as a b jet; the b-tagging efficiency is therefore a very important parameter.

2 Facilities

2.1 Electron-Hadron Colliders

As discussed in Section 1.2, an ep decay affords a much cleaner decay environment than a pp collision. Electron proton collisions are an example of a deep inelastic scattering process (of the electron off the quarks inside the proton). The scale which can be explored by DIS is $1/\sqrt{Q^2}$, where Q^2 is the momentum transfer of the process. The only previous ep collider, HERA at DESY [11], had a Q^2 value around 10 times smaller than that of the LHeC, the weakest potential ep collider candidate (FCC-he is a factor of 10 larger again) [12]. This affords the opportunity to gain an unprecedented insight into the substructure of the proton.

In these collisions a plethora of particles are created, many of which subsequently decay. Hadrons are created due to quark confinement, and bosons are exchanged as force carriers between particles. In DIS, the proton is essentially 'smashed', and the energy of the collision is converted to new particles. This allows for the search for the new scalar, ϕ, due to the production of Higgs bosons

through vector boson fusion, which will then subsequently decay into a pair of scalars. The precision of an ep collision is beneficial to a signal such as this, which may be swamped in other background processes.

2.2 Machine Options

The three machines for which this study is performed are the LHeC (Large Hadron electron Collider), DL-LHC (Double Luminosity LHC) and the FCC-he (Future Circular hadron-electron Collider). As discussed, the motivation for studying this decay process at an electron-proton collider is the increase in resolution compared to pp colliders. The cross sections for each of these detector options will be obtained for a range of ϕ masses, and with sensible cuts in place. This will allow the feasibility of each set up to be measured, given the different ϕ masses. As the mass of ϕ is unknown, other than being constrained to less than half the mass of Higgs and twice the mass of the b-quark, the effect of the cuts performed will be investigated for each mass/machine option.

Obviously the machine that provides the largest cross section is the most desirable, however this may not be the most realistic set up that is likely to be attained. The LHeC machine is likely the machine to see development in the near future, as it is a relatively simple upgrade the already existing LHC infrastructure: namely adding a new 60 GeV linear electron accelerator. This upgrade can be operated alongside all other LHC experiments with no interference whatsoever. See the LHeC conceptual design report for more details [13]. All of the machine options in this study are assumed to consist of a 60 GeV electron beam with either a 7 TeV (LHeC), 14 TeV (DLHC) or 50 TeV (FCChe) proton beam. These machines have centre of mass energies of approximately 1300, 1800 and 3500 GeV respectively, Eq. 1.

$$\sqrt{s} = \sqrt{4E_pEe} \tag{1}$$

In the interest of time, only the FCChe machine was studied at the detector level, while the other machine options were studied at the parton and generator level. Table 1 shows a breakdown of some of the properties of the FCChe machine, as this was the primary set up that was studied.

Parameter	Unit	Protons	Electrons
Beam energy	GeV	50000	60
Normalised emittance	μm	$2.2 \rightarrow 1.1$	10
IP betafunction	mm	150	$42 \rightarrow 52$
Nominal RMS beam size	μm	$2.5 \rightarrow 1.8$	$1.9 \rightarrow 2.1$
Waist shift	mm	0	$65 \rightarrow 70$
Bunch population	10^{10}	$10 \rightarrow 5$	0.31
Bunch spacing	ns	25	25
Luminosity	$10^{33}\text{cm}^{-2}\text{s}^{-1}$	$18.3 \rightarrow 14.3$	
Int. luminosity per 10 years	[ab^{-1}]	1.2	

Table 1: Breakdown of some of the main properties of the FFChe machine. (Source: [14].)

2.3 FCChe Detector

Each machine will require a unique detector, due to the different energy ranges over which they operate; which is simulated using Delphes (Section 3.1). The different collider options each have their own unique detector properties, so the efficiencies, pseudorapitidy ranges, resolutions, along with many other variables are distinct in each simulation.

In particular, the FCChe machine was studied through to the detector level. In the interest of time, LHeC and DLHC were only studied preliminariliy at the parton/generator level. The FCChe Delphes card that was used throughout the analysis, which contains all of the variables pertaining to the detector performance (efficiencies, resolutions, tracking etc) was prepared by U. Klein et al [15]. This detector system is a 4π state of the art system, meaning that the interaction point is fully enclosed in a detector system, covering a pseudorapidity range from -6 to +6 (explanation of pseudorapidity will be given in Section 3.2). There is also a 3.8 T magnetic field inside the detector for the purpose of measuring particles momentum, which can be obtained by measuring their radius of curvature due to the Lorentz force.

The efficiency of the tracking and calorimeter systems can depend on the pseudorapidity range at which it is operating, as well as the energy and momentum of the particle in question. The hadron calorimeters (HCAL), as well as the electron calorimeter (ECAL) efficiencies were written into the Delphes card. An example the energy resolution of the hadron calorimeter (HCAL) an be seen in Eq. 2.

$$\begin{aligned}\sigma_{HCAL} = (2.5 \leq \eta \leq 5.9) \times \sqrt{E \times 0.3^2 + E^2 \times 0.01^2} \\ +(-2.2 \leq \eta \leq 2.5) \times \sqrt{E \times 0.4^2 + E^2 \times 0.01^2} \\ +(-5.5 \leq \eta < -2.2) \times \sqrt{E \times 0.4^2 + E^2 \times 0.02^2}\end{aligned} \tag{2}$$

Other such efficiencies must also be included for the various tracking systems. Another important quantity for the detector is the b-tagging efficiency. A fuller explanation of b-tagging will be given later, but it is essentially the measurement of what quark flavour a jet originates from. The b-tagging efficiency was assumed to be 70% in the final analysis, with a mistagging rate of 10%.

3 Analysis Framework

3.1 Simulation

Different stages of the process will be handled by different programmes throughout the analysis. The generation of the different possible events for the final state is handled by Madgraph5 [16] and FeynRules [17]. As the final state is satisfied by multiple different Feynmann diagrams, these must be counted so that the total cross section can be calculated. The number of processes are counted using FeynRules, and then passed to Madgraph5 to calculate the total cross section of the event. The next level of the analysis is the fragmentation of the quarks into jets or showers. This

is handled by Pythia [18], which will produce a jet of particles from the original quarks. In this analysis, a DIS modified version of Pythia was prepared by U. Klein et al [15], owing to the fact that the process in question is electron-proton collisions.

Then these jets are reconstructed using Delphes [19]. Delphes reconstructs the generated particle jets by simulating the trajectory through a detector system, with the effect of smearing the jets. Here the detector efficiencies and resolutions will affect how the jet is viewed, as will the choice of jet reconstruction algorithm and jet thickness. For the purpose of this analysis the anti-kt algorithm was used, with different jet thickness' used throughout the various stages of the analysis, to study the effects on jet reconstruction.

3.2 Kinematics

Particle collisions can be described by the constituent 4-vectors of each particle involved. Each particle has an assigned 4-vector, commonly the 4-momentum, which has components of energy and momentum, of the form

$$\mathbf{P} = (E, \mathbf{p}), \tag{3}$$

in natural units. The invariant mass of the system, which is Lorentz invariant, is then given by

$$M = \sqrt{(\mathbf{P_1} + \mathbf{P_2})^2}, \tag{4}$$

as a result of

$$m^2 = E^2 - \mathbf{p}^2. \tag{5}$$

So, in a decay process, the mass of the decaying particle can be obtained from the 4-momenta of the 2 daughter particles. This method was used throughout the analysis, to find the mass of ϕ, and also of the Higgs, as the primary variable used in Delphes is particle 4-momenta. In Figure 1, each b quark pair should have an invariant mass equal to the mass of ϕ, while the ϕ pair should have an invariant mass equal to the Higgs mass. This allows for a mass cut to be performed, either by restricting the invariant mass of the particle to being within a certain mass window from the parent, or by finding the pairs with the smallest difference in invariant mass and using these to reconstruct the parent particles.

4-vectors and invariant masses, as well as a number of other things such as histograms, can be handled by the data analysis library ROOT [20]. ROOT is a library of programmes and classes that can be used during particle physics experiments and was used extensively throughout the project as a powerful analysis tool.

Another kinematic consideration is the pseudorapidity of the jets. Pseudorapidity is a measure of the angle relative to the beam axis of the jets, with the functional form given by

$$\eta \equiv -\ln\left[\tan\left(\frac{\theta}{2}\right)\right]. \tag{6}$$

A display of the variation of pseudorapidity with the relative angle can be seen in Figure 2.

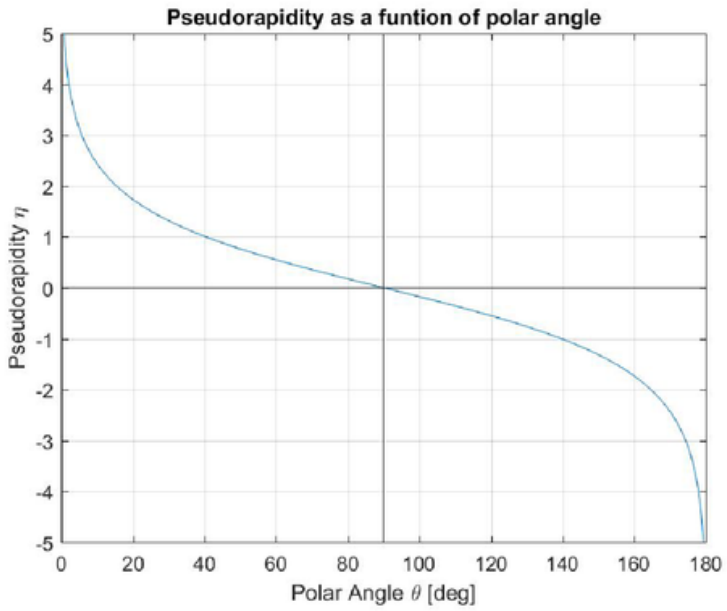

Figure 2: Variation of pseudorapdity with angle relative to the beam axis.

As the physical detector has a certain angular size, the jets must be measured within a certain pesudorapidity range (for example between -6 and +6 in FCChe). This imposes another cut on the signal process, as any jets outside of this range will not be measured, and must therefore be discarded.

The last cut which is of extreme importance is the transverse momentum cut, otherwise known as PT cut. The PT cut is closely related to the jet reconstruction which will be subsequently discussed in further detail. The reason for the inclusion of a transverse momentum cut is to eliminate small 'protojets'. These are jets that may be formed due to some QCD radiation undergoing hadronization, which is therefore not a 'real' jet resulting from the decay process itself [21]. These false jets can be formed if a particle inside the real jet emits a gluon in a direction away from the main jet. This gluon can then pair produce a pair of quarks, which then undergo fragmentation and hadronization and form a new smaller jet at an angle to the original jet. In this way, QCD radiation can cause an intrinsic background in the signal, by causing jet misidentification and potentially attributing false jets to the quarks in the decay process. As the protojets will have a smaller momentum than the signal jets, the PT cut acts as a safeguard in eliminating these false signals. However, it is unclear below what value jets should be discarded, so the effect of different PT cuts was studied.

As mentioned, further considerations such as the choice of jet reconstruction algorithm and

jet size play an important role on the reconstruction of the hadronized jets. There are many jet algorithms that can be used to piece together the spray of particles into a number of distinct jets, and each uses a different method. As the jets are the observable quantity in a particle collision, it is extremely important that they are reconstructed correctly, so that the parent particle can be correctly identified. The jet algorithm used in this analysis was the anti-kt algorithm, which uses sequential clustering to group the particles into jets [22].

This method measures the distance between particles, and groups them such that this distance is a minima, calling the result one jet. These distances are measured in transverse momenta space, at the Pythia and Delphes level and their must be included a minimum anti-kt separation. This corresponds to either 'fat' or 'slim' jets. There is no definitive correct value to use for the jet size: ATLAS uses a value of 0.6 [23] while CMS uses 0.4-0.5 [24]. Both fat and slim jets can lead to errors in jet reconstruction. Fat jets can cause the jets of 2 different parent quarks to overlap, and become merged into single high PT jet. While thinner jets can be split into multiple jets for a single quark, causing multiple low PT jets, that may be excluded due to low PT ($PT < PT_{cut}$) or counted as 2 separate jets when in fact they originate from the same quark. This is why the effects of different jet sizes were studied.

Another kinematic observable of particle collision experiments is the cross section. A cross section is an area (typical units of pico/femto barns) which quantifies the probability of a certain event. In a beam-target experiment, the probability for a collision is the ratio of the area of the particles to the area of the target. It is a result of this that the cross section corresponds to a probability of sorts. In DIS, the cross section depends on the partons inside the proton, as the energies are high enough that the electron hard scatters off the constituents of the proton [25].

Partons are the gluons and quarks that make up the substructure of the proton. The uud quark structure is only the valence parton structure, there is also a sea of inner partons that can only be probed at higher and higher energies. This quark-gluon sea is formed due to pair production and annihilation. The quarks are bound by gluons, which can pair produce sea quarks, which can in turn annihilate and create another gluon and so on [26]. As a result of this, the inner structure of the proton is very dynamic and cannot be described exactly: hence they are described by parton distribution functions. The parton distribution function used in this analysis was primarily the CTEQ6L1 PDF [27], however NNPDF23 [28] was also used to illustrate the dependence on PDF (Section 4.2). The PDF also effects the cross section of the process, which is given by

$$\frac{d\sigma}{dQ^2} = \frac{4\pi\alpha^2 Q_q^2}{Q^4}\left[(1-y)+\frac{y^2}{2}\right]\sum_q e_q^2 q^p(x)dx, \tag{7}$$

where $d\sigma/dQ^2$ is the differential cross section of a deep inelastic scattering process of energy Q^2, y is a Lorentz invariant quantity defined as $y = p_2.q/p_2.p_1$, which is related to fraction of energy lost by the electron in the scattering process [29]. Other than the rest of the numerical factors, the final variable which is of great importance is the parton distribution function, given by the summation

term. The PDF can be measured by measuring the structure functions of the proton, and using the relation

$$F_2^p(x,Q^2) = 2xF_1^p(x,Q^2) = x\sum_q e_q^2 q^p(x). \tag{8}$$

The structure functions are related to the charge and spatial distributions of the protons substructure [30]. These are able to be measured by experiment, and using Eq. 8 the parton distribution functions can be measured. These measurements are extremely difficult however, so there are many competing models and parameters available.

Finally, the cross section is related to the luminosity of the accelerator simply as the ratio between number of detected events and cross section, Eq. 9.

$$L = \frac{1}{\sigma}\frac{dN}{dt} \tag{9}$$

The integrated luminosity is then the integral over time, and commonly has units of inverse fb. The integrated luminosity gives an indication of how many events of a process with a certain cross section you are likely to see in the run time of the experiment. It is therefore an important quantity in any particle physics experiment. In this analysis, a luminosity of 100 fb^{-1} per year was assumed for the FCChe machine.

4 Benchmarking Procedure

4.1 Coupling Strength and Branching Ratios

When a particle decays, it produces a distribution known as the Breit-Wigner distribution. This is a probability density function which describes the energy of the decay products [31]. The sum energy of all the decay products will be close to the energy of the particle which decayed to produce them, so the peak of the Breit-Wigner distribution will be centred around the mass of the parent particle, similar to the invariant mass using the 4-momenta. This is known as a resonance, and the form of the Breit-Wigner distribution is

$$f(E) = \frac{1}{(E-E_0)^2 + \frac{\Gamma^2}{4}}. \tag{10}$$

The width, Γ, of the distribution is the full width at half maximum, which is an expression of the uncertainty in the energy of the decay process. This uncertainty is then related to the lifetime of the particle via the uncertainty principle [31]. So, with units of $\hbar$=1, the lifetime of the decay process is then given by

$$\tau = \frac{1}{\Gamma}. \tag{11}$$

Dividing the partial width by the total width of the parent particle gives the branching ratio (BR) of the process, Eq. 12. The branching ratio is the fraction of the time that the parent particle decays into a specific daughter particle.

$$BR = \frac{\Gamma_{partial}}{\Gamma_{Total}} \tag{12}$$

So the branching ratio of $h \to \phi\phi$ can be calculated by dividing the partial width of the process by the total width of the Higgs. Similarly, the partial width of $\phi \to b\bar{b}$, divided by the width of ϕ gives this branching ratio. For this analysis, the width of ϕ was assumed to be equal to the width of the SM Higgs. This is a reasonable assumption due to the expected narrow width for ϕ, as the Higgs total width is also extremely narrow (4.07×10^{-3} GeV) [32].

The two branching ratios, $\mathrm{Br}(h \to \phi\phi)$ and $\mathrm{Br}(\phi \to b\bar{b})$, were set to 10% and 100% respectively. The decay of Higgs into exotic particles has a constrained branching ratio of $\mathrm{Br}(h \to BSM) = 30\%$ at 95% CL [33], so $\mathrm{Br}(h \to \phi\phi) = 10\%$ is a good place to start searching for these BSM decays. Assuming ϕ has the same branching ratios as the Higgs, the decay into a $b\bar{b}$ pair would be heavily dominant; as for low mass Higgs models, the branching ratio of $h \to b\bar{b}$ approaches around 85% [34]. Figure 3 illustrates the fact that $b\bar{b}$ decays are dominant for Higgs masses in the range of around 100-200 GeV, while the branchings into other particles are much smaller. This was the basis for neglecting the other branching's and setting $\mathrm{Br}(\phi \to b\bar{b})$=100%.

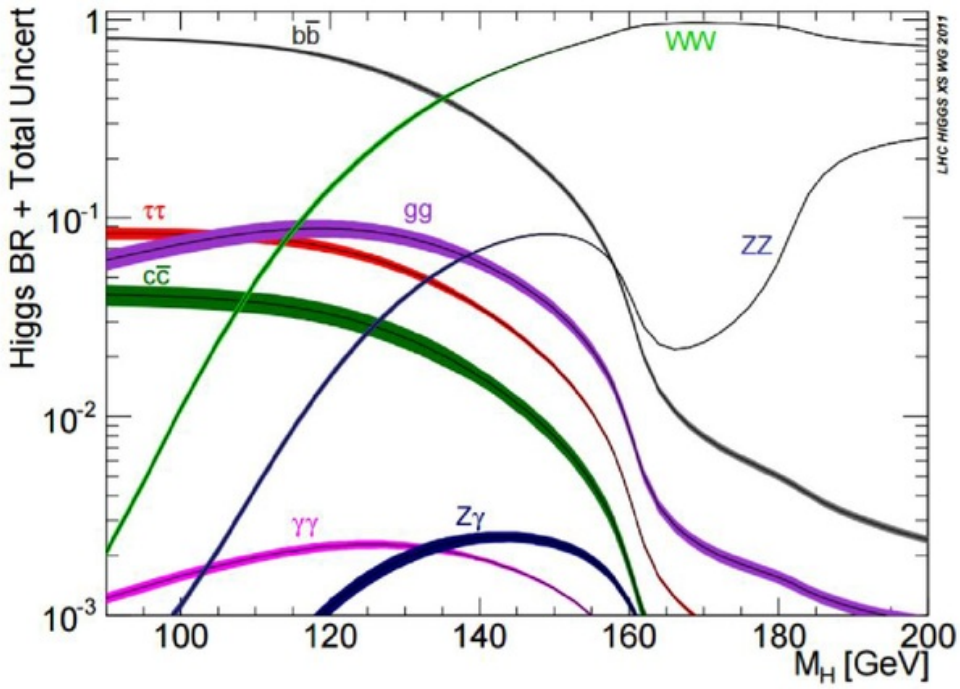

Figure 3: Variation of Higgs branchings ratios for different Higgs mass hypotheses. (Source: [34].)

As discussed, for low mass Higgs', decay into $b\bar{b}$ is dominant and it is assumed that ϕ follows the same branching's. Assuming the two branching ratios of $h \to \phi$ and $\phi \to b\bar{b}$ to be 10% and 100% respectively, these numbers provide a reasonably well constrained landscape in which to perform the preliminary search, while no stronger figures are available. The decay of the Higgs into ϕ in this model was controlled by the mass dependent coupling parameter Ahss. It was therefore necessary to scale the value of Ahss, depending on the mass of ϕ, to achieve the correct BR of 10%. This is due to the fact that the mass of ϕ is relatively unconstrained (less than half the Higgs mass but greater than twice the b quark mass are the only constraints). Therefore, the analysis was performed over a range of masses to scan the whole phase space.

To scale the coupling accordingly, Madgraph5 was run with the single process of $h \to \phi\phi$, with any arbitrary value of Ahss. The partial width of the process was returned and using Eq. 12 the branching ratio obtained. This value could then be used to scale Ahss according to the desired branching ratio, using

$$Ahss_{new} = \sqrt{{Ahss_0}^2 \times \frac{BR_{new}}{BR_0}}. \tag{13}$$

The form of Eq. 13 results from the fact that the cross section, σ, is proportional to the coupling constant squared. Here, $Ahss_0$ is the value used in Madgraph5 to generate the partial width/branching ratio BR_0. This is then used to scale to the desired branching ratio, BR_{new} (10%), and obtain the value of Ahss required. Figure 4 shows the variation of this coupling parameter with branching ratio for a range of different ϕ masses. The same procedure was also applied to the coupling parameter that controls the decay of ϕ into a $b\bar{b}$ pair, ysbb. The variation of this parameter can be seen in Figure 5.

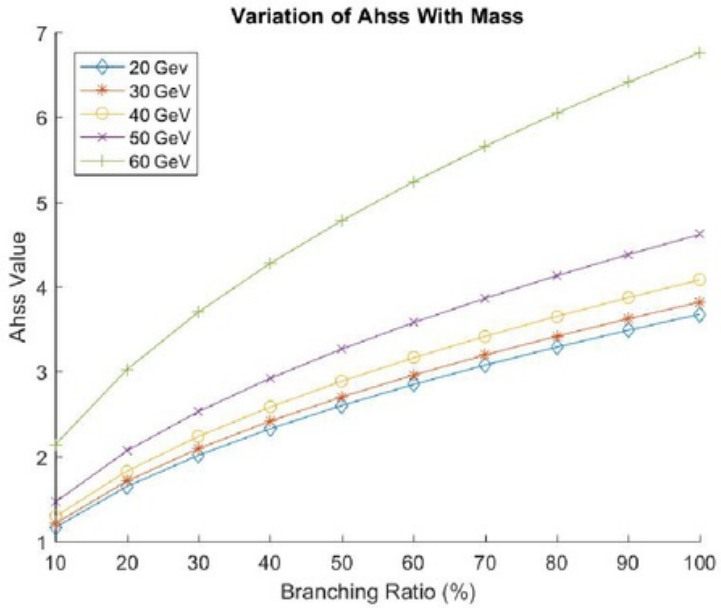

Figure 4: Variation of the Ahss coupling parameter, responsible for determining $\mathrm{Br}(h \to \phi\phi)$, for different branching and scalar mass scenarios.

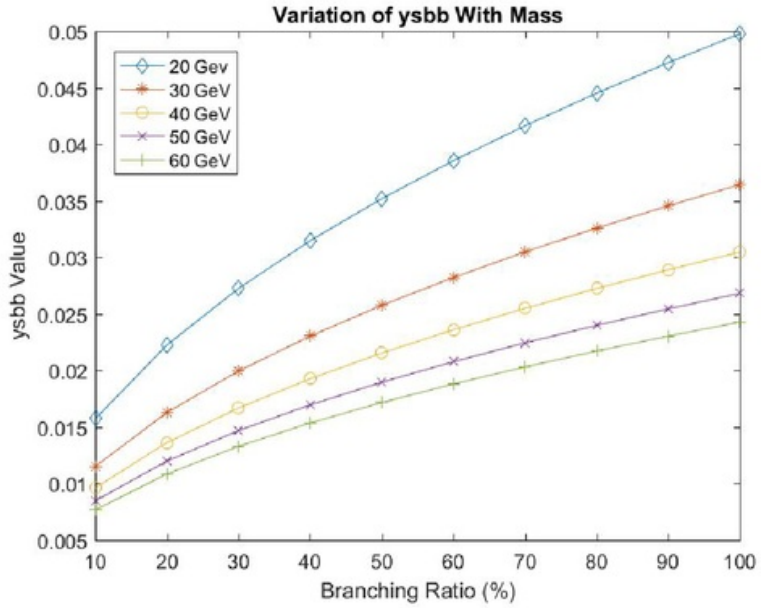

Figure 5: Variation of the ysbb coupling parameter, responsible for determining $\mathrm{Br}(\phi \to b\bar{b})$, for different branching and scalar mass scenarios.

Both of the coupling parameters that define the process show non-linear variation with cross

section. Their form is most likely quadratic in nature, resulting from the relationship of cross section to coupling squared. This procedure was performed to obtain the values of Ahss and ysbb that respectively give branching ratios of 10 and 100 %, however another study using both branching ratios at 100% was also performed, which will be discussed later as a test of both methods accuracy. Another study was performed with the coupling between the Higgs and ϕ set to extremely small values, to see the feasibility of detecting ϕ, given a smaller branching fraction than 10%.

4.2 Cross Sections and Mass Dependence

Using the correctly normalised couplings for each mass, the generator level cross sections were calculated for each beam energy and over a range of masses (20-60 GeV). These cross sections were produced with no transverse momenta cuts and in a pseudorapidity range of -6 to +6. No electron beam polarisation was included in this level of generation, which would just have the effect of multiplying the cross section by a constant factor. In addition, the effect on the signal cross section due to PDF choice was also studied. This was done by performing the analysis with 2 different PDF's, namely NNPDF23 and CTEQ6l1. These PDF's are the parton distribution functions, which are probability density functions that give the probability of finding a parton with a given momentum at a given scale of resolution. The results of this can be seen in Figure 6.

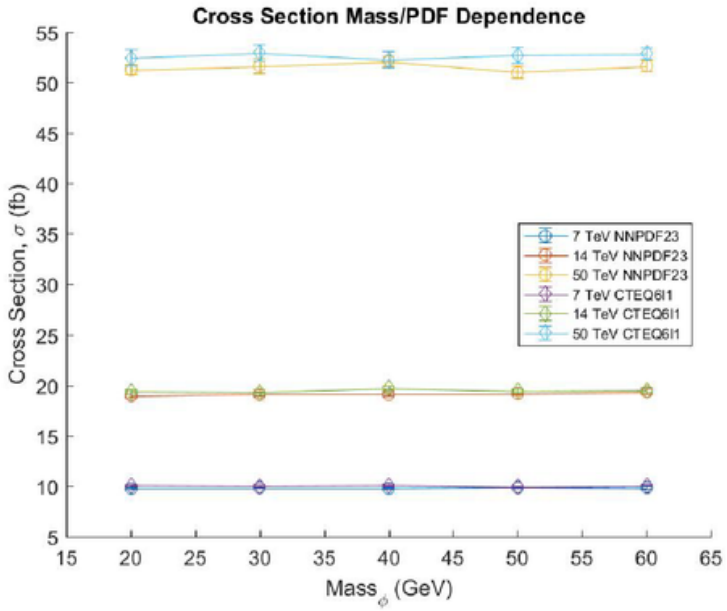

Figure 6: Variation of generator level cross section with both scalar mass and PDF.

The variation of cross section with ϕ mass, as well as with PDF, is shown to be flat, within statistical fluctuations. This is expected as the cross section will only vary as a function of the branching ratio of the Higgs into ϕ and of ϕ into $b\bar{b}$. As these couplings were scaled with mass

to achieve the desired branching ratio, all the cross sections should be equal to within statistical differences. Therefore, the cross section's should all be equal to one tenth of the total Higgs cross section at each machine, resulting from the fact that Br($h \to \phi\phi$)=10% and Br($\phi \to b\bar{b}$)=100%. If the decay of ϕ into a pair of b's was not set to 100% this would not be the case however, but with these figures, one tenth of all Higgs' will decay into a $b\bar{b}$ pair. This is why the generator level cross section should be independent of mass. Once cuts are applied this will no longer be the case however, as the effect of the various momentum and η cut's on the cross section will depend on the mass of ϕ.

Another method of rescaling the cross sections was suggested by Chen Zhang et al [35], namely, calculating the cross section with Br($h \to \phi\phi$)=100%. This cross section was then again divided by 10 to get to the cross section corresponding to BR=10%. This was tested by comparing the results using this method to the method of rescaling the couplings themselves before calculating the cross sections. Table 2 shows the agreement between both methods.

		Beam Energy (TeV)			Scaled Up (x10) from BR=10%			Percentage Difference		
	Mass (GeV)	7	14	50	7	14	50	7	14	50
Cross Section (fb)	20	98.19	190.7	516.5	97.6	191.1	516.6	0.604508	-0.20931	-0.01936
	30	98.21	191.1	517.9	97.7	191	520.9	0.522006	0.052356	-0.57593
	40	98.19	191.5	516.9	98.3	190.9	518	-0.1119	0.314301	-0.21236
	50	98.43	190.8	518.5	98.5	191.2	516.4	-0.07107	-0.20921	0.406662
	60	98.42	191.9	517	98.3	190.9	516.6	0.122075	0.523834	0.077429

Table 2: Comparison between both methods of either 10% branching or 100% branching ratio scaled down, for each machine option.

Table 2 shows that either method of scaling the cross sections, either by first scaling the couplings or scaling the cross sections at the end should give the same result (to within $< 1\%$). Another check of this method was performed. By varying the coupling of Ahss such that a BR of 10, 20, 30,..., 100% was achieved, a plot of cross section vs. branching ratio was produced. This was done with a single mass value for ϕ, as Figure 6 and Table 2 show that the cross sections should be independent of mass. The value of ysbb was set to BR=100% in every case. Figure 7 shows how the cross sections varied with branching ratio.

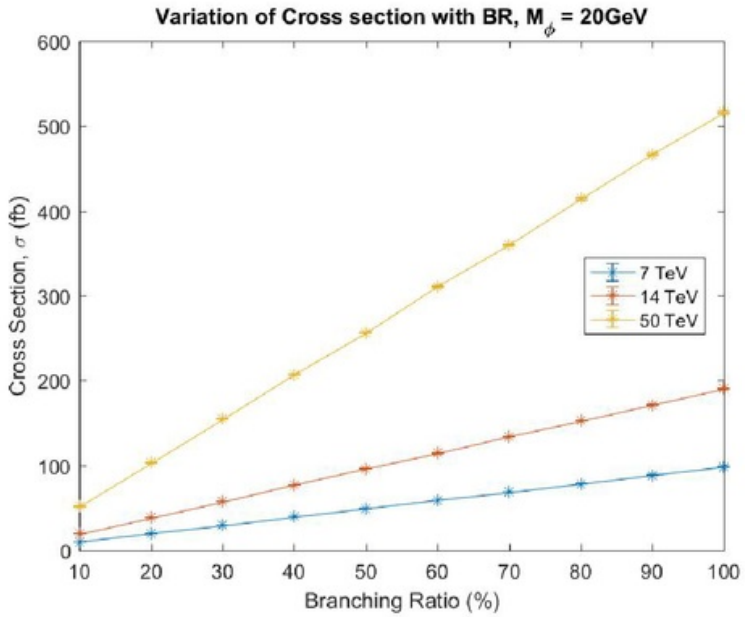

Figure 7: Variation of cross section with Higgs to ϕ branching ratio from 10-100%, for each machine option for M_ϕ=20 GeV.

Figure 7 shows that the cross section can be scaled according to the strength of the coupling parameter in a linear fashion. This study was also continued down to extremely small couplings, not as a test of the linearity of the methods, but to check the cross sections that could be obtained with exceptionally small coupling of h and ϕ. This was done with mass equal to 20, 40 and 60 GeV, however, at this level there is no mass dependence so the 20 GeV results are displayed herein. Table 3 and Figure 8 show the results of this analysis.

Mass (GeV)	Ahss	BR (%)	Energy (TeV) 7	14	50	7	14	50
			σ (fb)			Δσ (fb)		
20	0.1643	0.2	0.021	0.401	1.06	0.001	0.00	0.01
	0.2598	0.5	0.052	1.007	2.65	0.002	0.005	0.01
	0.3674	1	1.042	2.00	5.32	0.005	0.01	0.02
	0.5195	2	2.093	4.01	10.53	0.009	0.02	0.04
	0.6363	3	3.12	5.98	15.86	0.01	0.03	0.07
	0.7347	4	4.15	7.95	21.1	0.02	0.04	0.1
	0.8215	5	5.18	10.00	26.4	0.03	0.06	0.1
	0.8999	6	6.22	12.02	31.6	0.04	0.07	0.2
	0.9720	7	7.3	14.03	37.1	0.03	0.06	0.1
	1.0391	8	8.38	16.06	42.2	0.04	0.08	0.2
	1.1021	9	9.45	18.08	47.9	0.04	0.07	0.2
	1.1617	10	10.46	20.05	53.1	0.05	0.09	0.2

Table 3: Cross section variation for Higgs ϕ coupling from 0.2% to 10% at each collider option.

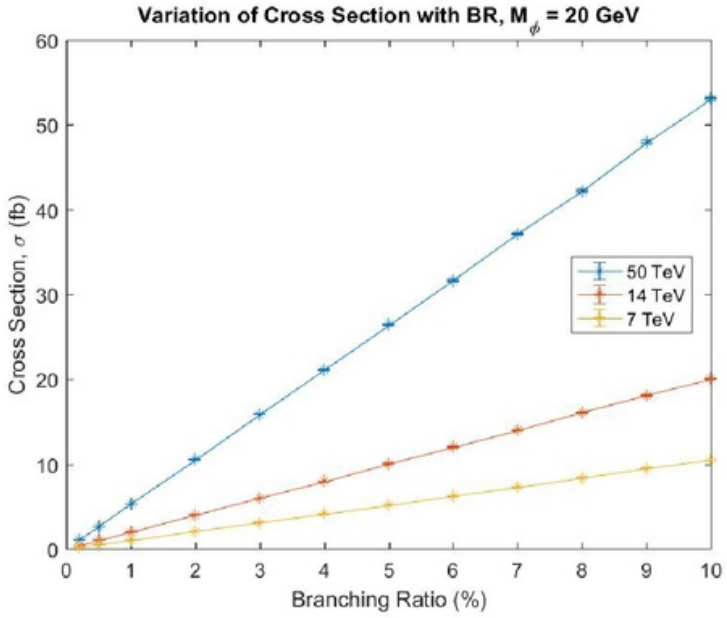

Figure 8: Variation of cross section with Higgs to ϕ branching ratio from 0.2-10%, for each machine option for M_ϕ=20 GeV.

The lowest branching ratio was set to 0.2%. At this level the FCC-he collider still obtains a cross section of 1fb, while the others are smaller. The 1fb level could provide enough of a signal to be useful, however this is at the generator level: once cuts are applied this signal would likely become too small and be lost in the background processes.

4.3 Parton-level Studies for Signal Process

As discussed, the lower the mass of ϕ the more sensitive the study will be to transverse momenta cuts. This is due to the fact that the lower mass ϕ is more likely to have low PT jets, which will be discarded if they are below the chosen cut. Therefore the acceptance's of the 20 GeV scalar were investigated in particular, as this will be the most sensitive. The geometric acceptance is the ratio of the signal cross section with cuts in place, to the signal cross section with no cuts,

$$A = \frac{\sigma_{cuts}}{\sigma_{tot}}. \tag{14}$$

Table 4 shows a crude acceptance scan done at the generator level with different transverse momenta cuts for the 20 GeV scalar. A better scan would be obtained at the reconstructed level, after the jets are reconstructed after undergoing hadronization. This level of analysis comes later however, once the generated events have been passed through Pythia and Delphes.

pt cut	Cross section (fb)	Error	Acceptance (%)
0	10.71	0.1	100
5	8.03	0.08	75.0
10	4.46	0.07	41.6
15	1.87	0.05	17.5

Table 4: Effect of increased PT cuts on the generator level cross section for M_ϕ=20 GeV at LHeC.

A pseudorapidity scan was also performed to see how the psueodrapidity range of the b quarks effects the cross section of the result. This gives an idea of the distribution of the b quarks relative to the forward beam. The detector set up covers a pseudorapidity range from -6 to +6 at FCChe as discussed. Figure 9 shows the pseudorapidity acceptances for: no momentum cuts, 5 GeV cuts and 10 GeV cuts for the b partons. This helps to see how the momentum cuts, in conjunction with the pseudorapidity cuts, effect the cross section.

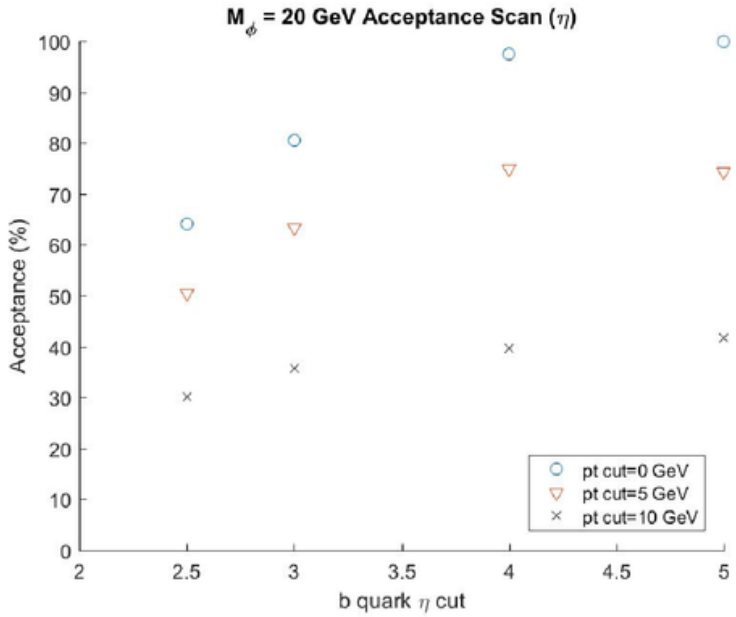

Figure 9: Effect of different η cuts in conjunction with different PT cut scenarios, for M_ϕ=20 GeV at LHeC.

The pseudorapidity acceptance is most noticeable with no transverse momentum cuts in place. The combined effect of an η cut of less than 2.5 and a PT cut of 10 GeV results in an acceptance of around 30%.

5 Detector-level Studies

Once the benchmarking procedure was complete, the next stage of the study was the preliminary analysis of the jets. This point in the analysis was done at the Pythia and Delphes level, moving away from the parton level and towards the final result. As discussed, due to time constraints, the primary focus was on the FCChe machine. Given a larger time budget the other machines could have been investigated at this level, but as the FCChe is the highest energy machine, to an approximation, the results could be scaled down to the lower energy machines, whereas the low energy results could not be scaled up; hence the focus was set on FCChe.

The aims of these studies were to study all the cuts and analysis strategies that will effect the final signal. To do this, different codes were written to analyse the delphes.root files produced in the event generation. ROOT was used extensively at this level of the study, as it contains many useful classes and modules for the analysis, as well as histograms. Cuts and conditions could then be placed on the signal, at the jet level, having the advantage of a much more sophisticated level of analysis, as many different studies can be performed and the effects of different cuts explored. This was also the technique used to perform the jet recombination analysis, i.e. combining the jets (the

observable quantities in the experiment) in such a way as to reconstruct the scalars.

5.1 Sensitivity to b-tagging Pseudorapidity Range

As discussed in Section 4.3, a study of the b-tagging range's effect on acceptance was done once the partons had undergone hadronization and fragmentation. The heavy flavour association was set at 3 and 5 in pseudorapidity and the number of b-tagged jets measured. Figure 10 shows the number of b-tagged jets at the generator level.

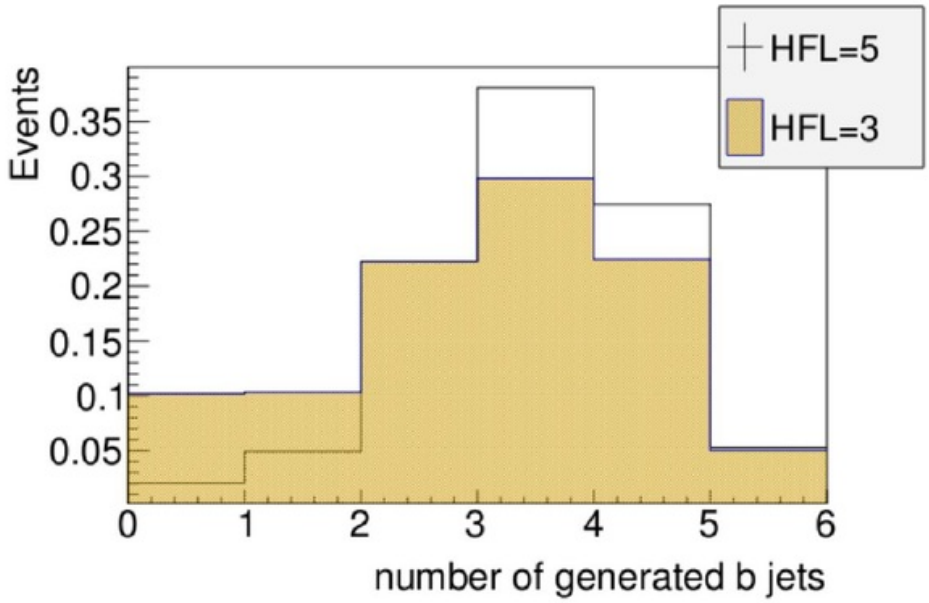

Figure 10: Normalised distributions showing the number of b tagged generated jets with HFL set to 3 and 5 respectively.

The same trend as above is also seen at the reconstructed (Delphes) level. This is an intuitive result as a greater tagging range should increase the number of tagged jets. However, b-tagging becomes more difficult the closer it approaches to the beam axis. This is a result of the methodology used to tag b-jets. B jets can be identified by their long lifetime, but not as long as hadrons of lighter quarks: having lifetimes long enough such that they will decay inside the detector. This causes secondary vertexes, which can be used to indicate the presence of a b-jet. As the pseudorapidity increases however, it approaches the main beam, which has extremely high energy. This limits the precision by which the secondary vertices can be located, and hence inhibits b-tagging. LHCb however has shown that b-tagging can be done all the way up to a pseudorapidity of 5 [36].

Another problem with increased b-tagging range is that it may not effect the signal beneficially. The b quarks resulting from the decay of the scalar will mostly have a pseudorapidity in the range

0-4 (as seen in Figure 11) so extending the b-tagging range may pick up high η b-jets that are not part of the signal process: adding more of an intrinsic background than signal.

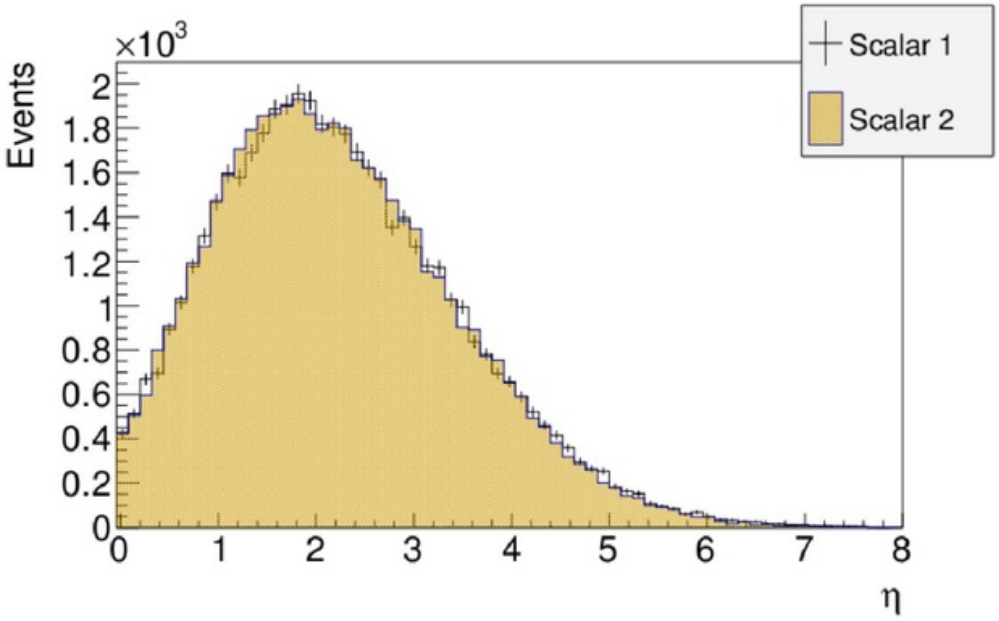

Figure 11: Average η distributions of each b-quark pair (scalar).

Figure 11 shows that most events take place between around 0-4 in pseudorapidity. Even with increased b-tagging range, better results may be obtained with tighter pseudorapidity cuts, due to the fact that more signal like events may take place in a tighter η range compared to the dominant backgrounds. Tighter η requirements can also decrease the likelihood of picking up forward b-jets and considering them part of the decay process. The effect of pseudorapidity range will be considered later, when dealing with the signal to background ratios and how it can be maximised. This discussion will be continued in Section 7.1.

5.2 Invariant Mass Study (Combinatorics)

As the 4b jets originate, firstly from the 2 scalars, and secondly from the Higgs, m_{2b} should be close to the scalar mass, while m_{4b} should be close to the Higgs mass. However, as the mass of the scalar is unknown presently, this condition could not be used as a constraint. It could, assuming the scalar mass for each different mass study, but this would be effectively jumping to the answer: as in the real experiment the mass is unknown so cannot be used as a constraint on jet combinations.

Instead of using this technique, the method used was to find the quark/jet pairs that have the most similar invariant mass, and using these combinations as the 2 scalars. To elaborate, using 4 jets for example labelled 1-4, the different combinations of jet pairs were calculated (1+2 & 3+4, 1+3 & 2+4, 1+4 & 2+3). Out of these 3 sets, the set with the most similar invariant mass was

used to reconstruct the scalar mass, with a further condition, that the mass must be larger than twice the mass of the b quark, so around 8 GeV. Then the mass of the 4 jets should be close to the Higgs mass, so there should be a peak around 125 GeV in the 4-jet mass distribution.

At an early stage in the analysis, the above technique was used to reconstruct the jet pairs, taking the 4 highest PT pairs and performing the combinatorics. Another analysis method that was pursued was taking the combinatorics of all jets in an event, using the method outlined earlier but upto N jets. At the parton level, the scalar and Higgs masses reconstructed almost perfectly using each method, as would be expected as this is a parton level process, i.e. no fragmentaiton or hadronization. An example of these parton level di-jet mass distributions can be seen in Figure 12.

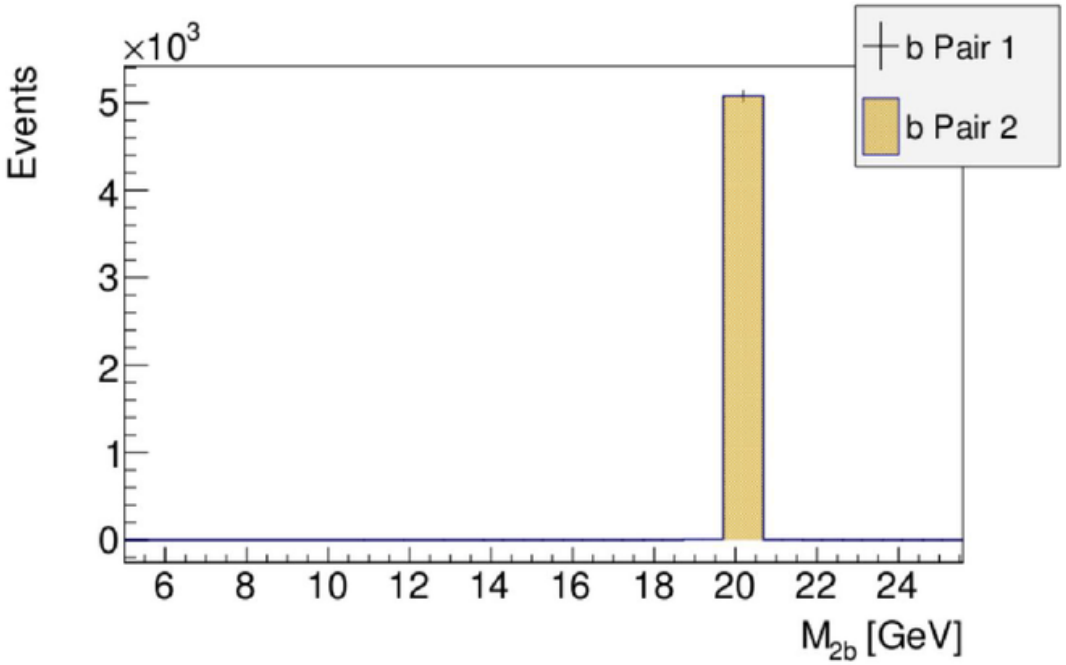

Figure 12: Invariant mass of each $b\bar{b}$ pair, for the 20 GeV signal sample with FCChe.

As expected for a purely parton level process, the invariant mass peaks are much more precise than would be seen for a jet level process. The same trend is seen for the 4b invariant mass, a 125 GeV needle corresponding to the Higgs (2b's make a scalar and 2 scalars make a Higgs).

The updated method performed all the different jet combinatorics upto N jets, for each individual event at the generated and reconstructed level. Even though the pure decay event should be a 5 jet event, due to the fragmentation and jet reconstruction techniques, higher (and lower) numbers of jets are not only possible but quite likely. This was done using a series of nested for loops to loop over each jet combination, while making sure each jet can only be used once per check. The jets with the closest invariant mass were chosen as the pair resulting from the scalar, again with the condition that there must be a minimum mass of around 8 GeV, and a generous maximum mass of

70 GeV (just over twice the Higgs mass). Figure 13 illustrates how the method worked to check the jet combinations.

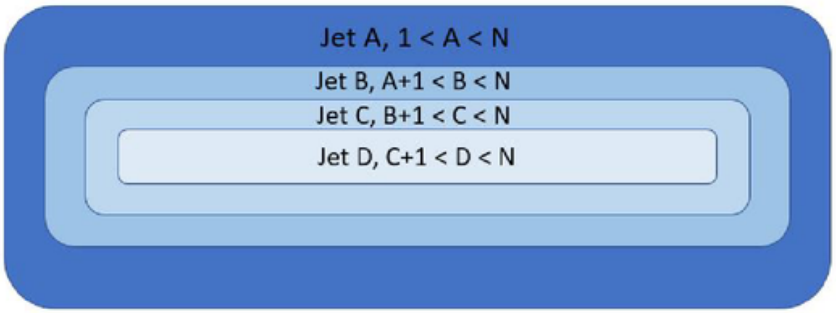

Figure 13: Jet A varies from 1 to the number of jets, N, while each subsequent loop varies from +1 of the loop before it, to N. Each loop is completed at each succesive iteration of the loop it is inside and the mass difference of the jets is calculated at the level of jet D so that all the jet combinations are made with no double uses of jets.

The initial dijet mass difference was set at 10 GeV, then every time a smaller dijet mass difference is obtained, we store this difference and assign these jets as our dijet pairs. Then each iteration measures the mass difference against the minimum, and if it is lower we then rewrite these jets as the pairs and so on. The final dijet pairs then have the smallest mass difference out of all possible combinations. Another cut that was imposed while doing the combinatorics was that the ΔR of the pairs should be minimum, along with the mass difference of the pairs being minimised. ΔR is a variable relating to the conical size of the jet in η/ϕ space.

$$\Delta R = \sqrt{\Delta\phi^2 + \Delta\eta^2} \tag{15}$$

The reasoning behind the minimisation of this variable is that the $b\bar{b}$ pair should both originate from the same scalar, and therefore should be close to one another. In the case of the 20 GeV scalar for example, the initial minimum for ΔR was set at 2, and minimised from this. Two was found to be optimal as it is large enough to leave enough jet possibilities to try out but not too large to let in too much background (b pair's from backgrounds may have larger ΔR's as they don't necessarily originate from the same particle decay, e.g. the supersymmetric scalar). This cut was not optimal for each mass case however, as will be discussed in Section 5.3. The generator level ΔR cut was 0.4 in every case, i.e. this is the minimum separation between objects to be considered as jets. The justification for using a value of 0.4 will be explained in Section 5.4.

An example pair of di-jets obtained using this combinatorics method with the stated cuts can be seen in Figure 14.

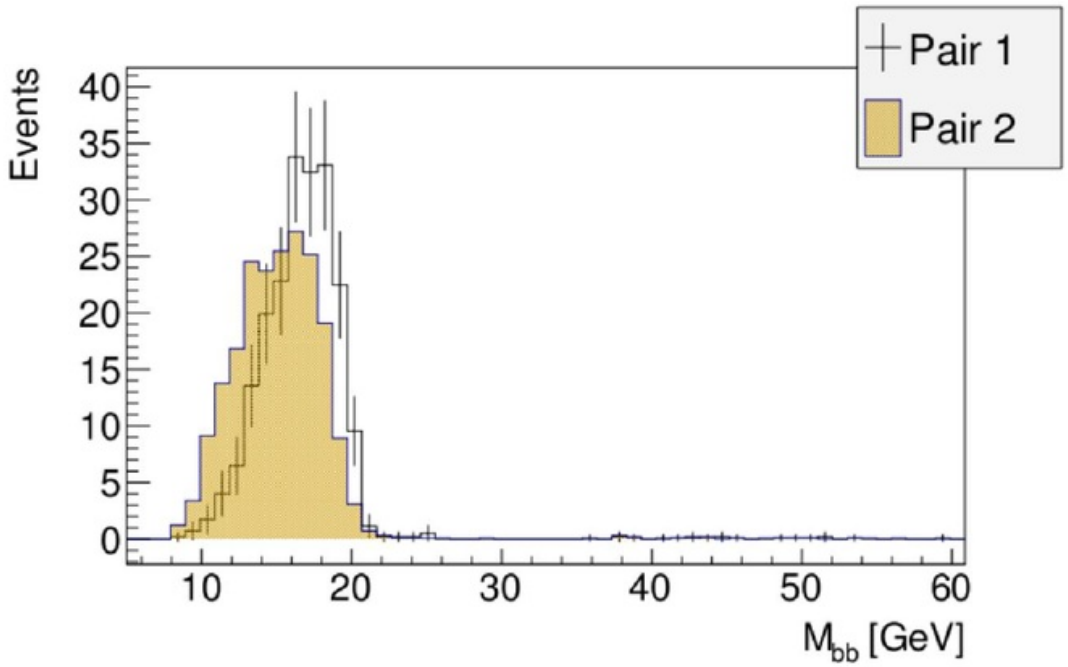

Figure 14: This overlay shows the reconstructed jet pairs invariant masses using the combinatorics method, for $M_\phi = 20$ GeV at FCChe.

Note that the above plot shows the dijet pairs with the condition that both jets in each dijet are b-tagged, for the signal process at FCChe. Numerous different scenarios with varying numbers of b-tags were performed, this figure is to illustrate the accuracy of the method Both reconstructed dijet pairs are in relatively good agreement with one another, with pair 2 being slightly shifted to lower masses. They both have a shoulder at 20 GeV, which is what would be expected for a 20 GeV scalar resonance.

An example of the 4-jet mass distributions obtained by taking the sum of the two chosen scalar pairs can be seen in Figure 15. Again, this distribution was obtained from 4 b-tagged jets. Note, at this point in the analysis, the b-tagging efficiency was set to 1. These plots are for demonstrative purposes to illustrate the method of jet reconstruction via combinatorics; a more realistic b-tagging efficiency was explored at a later point in the analysis, once the methodology was understood.

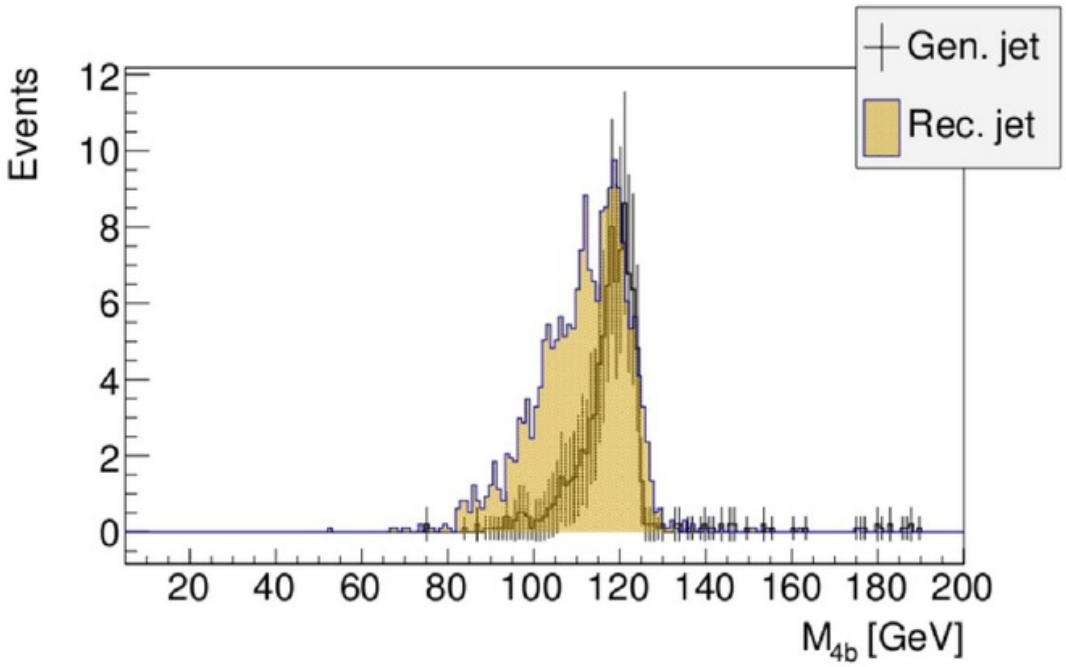

Figure 15: 4b mass distributions at the reconstructed and the generated level, for M_ϕ=20 GeV at FCChe.

There is good agreement between the reconstructed 4b mass distribution and the generated. The reconstructed distribution is broader and has fewer counts, which is to be expected due to smearing from the detector resolution.

5.3 Pseudorapidity Study

It would be expected that the jets originating from the scalars should be close to one another in η/ϕ space. This was the assumption behind the ΔR cut outlined in the combinatorics method. Figure 16 shows the ΔR distribution for the 20 GeV scalar in particular.

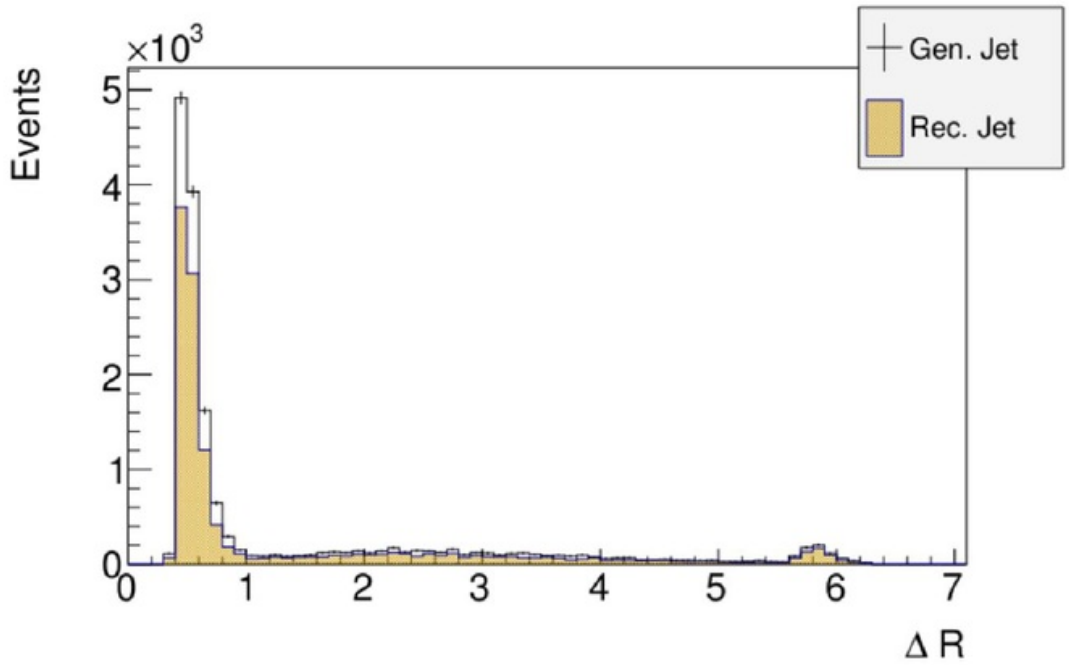

Figure 16: ΔR separation of the different levels of analysis for the 20 GeV scalar at FCChe.

At the jet level of analysis (for M_ϕ=20 GeV), most events occur at a ΔR of less than 2: which was the justification for the use of 2 as a starting point in the jet combinatorics. However, for different masses the ΔR distributions were found to be significantly different; meaning that while a ΔR cut of 2 may be optimal for the 20 GeV case, it may not be for other masses. Figure 17 shows how the ΔR varied for each different mass option.

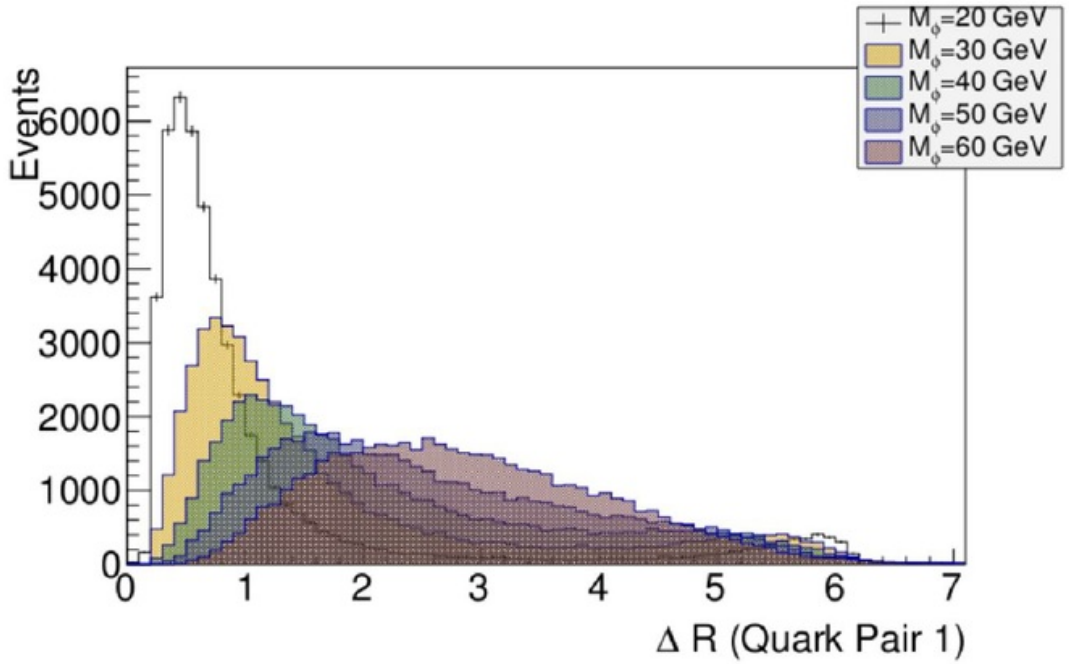

Figure 17: ΔR values between the quarks of the first dijet pair formed for different mass scenarios at FCChe. Similar distribution seen for the second quark pair (Figure 55 in the Appendix).

Clearly each mass option has very distinct ΔR distributions, increasing in ΔR as mass increases, which means that the starting cut when doing the combinatorics may need to be re-evaluated. This overlay was produced using the quark ΔR distributions, i.e. the 'true' distribution. To further help classify the signals, the η and ϕ distributions were studied separately. Figure's 18 and 19 show the difference in η and ϕ respectively between each b jet in the scalar pair.

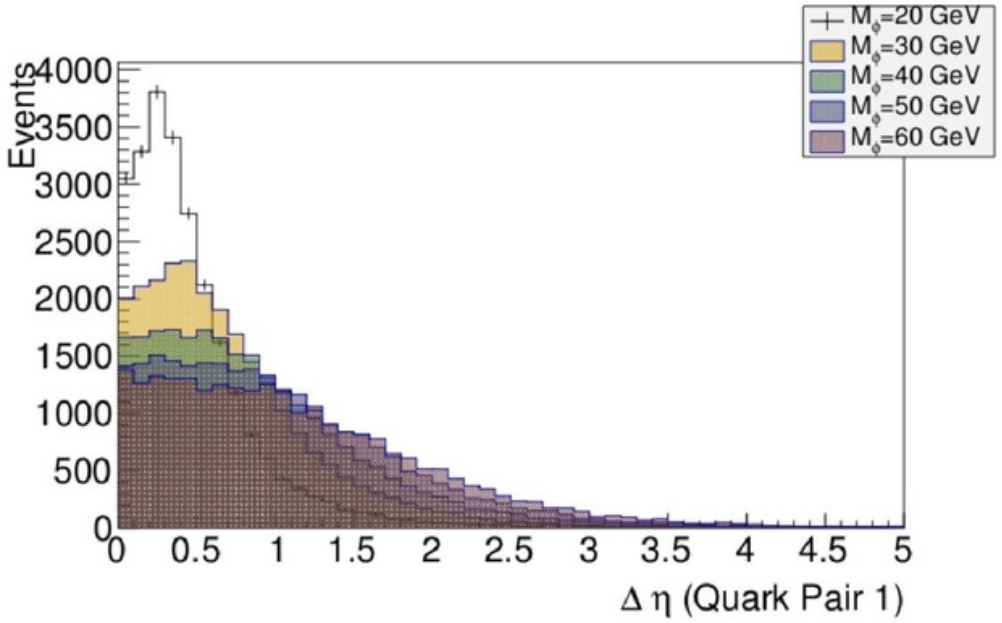

Figure 18: $\Delta\eta$ between each b jet in scalar 1 for different mass scenarios at FCChe. Similar distribution is seen for pair 2 (see Figure 56 in Appendix).

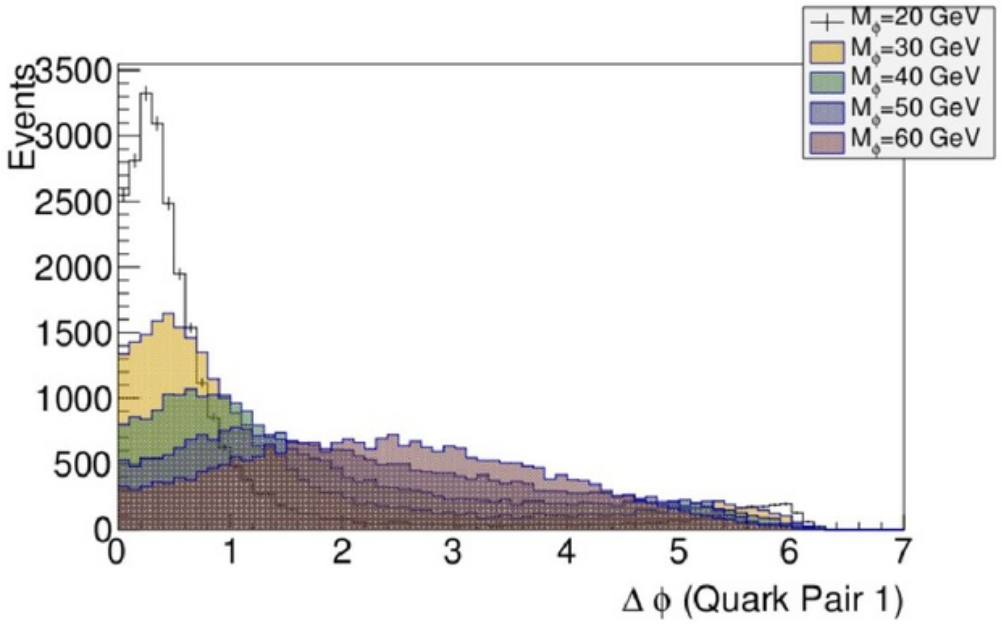

Figure 19: $\Delta\phi$ between each b jet in scalar 1 for different mass scenarios at FCChe. Similar distribution is seen for pair 2 (see Figure 57 in Appendix).

As can be seen from the above figure, the $\Delta\phi$ difference is driving the increase in ΔR with

increasing mass. $\Delta\eta$ is still relatively tight for each mass option (most events occurring at approximately $\eta < 2$). Next the separation in η and ϕ between each scalar pair was investigated. This gave topological information of how the scalars are distributed, in addition to the previous investigation of how the b's are distributed in each scalar. Figure's 20 and 21 display the difference in η and ϕ respectively between each scalar.

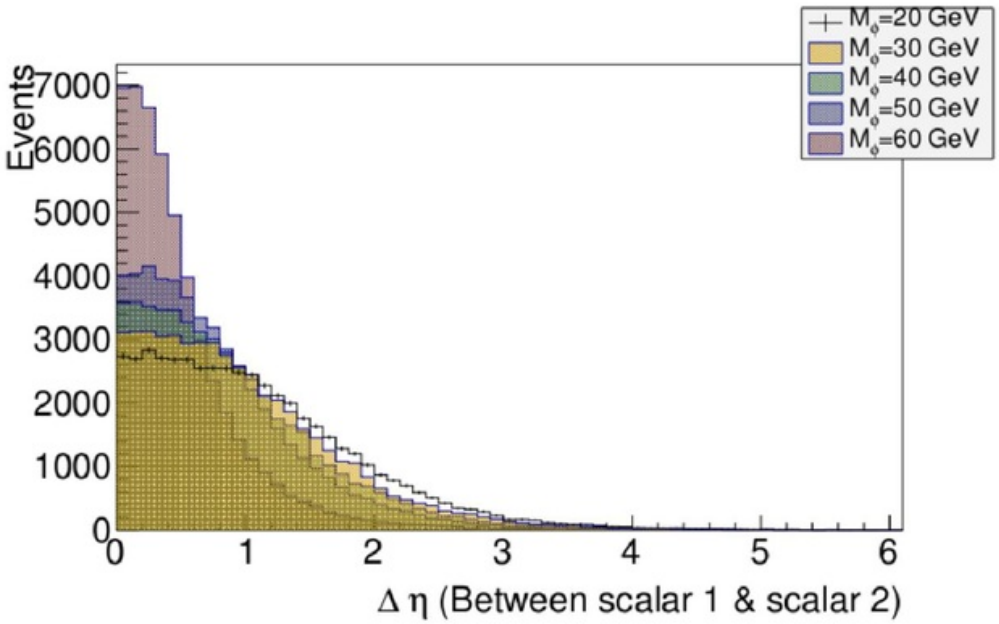

Figure 20: $\Delta\eta$ between each scalar pair for different scalar mass scenarios at the FCChe.

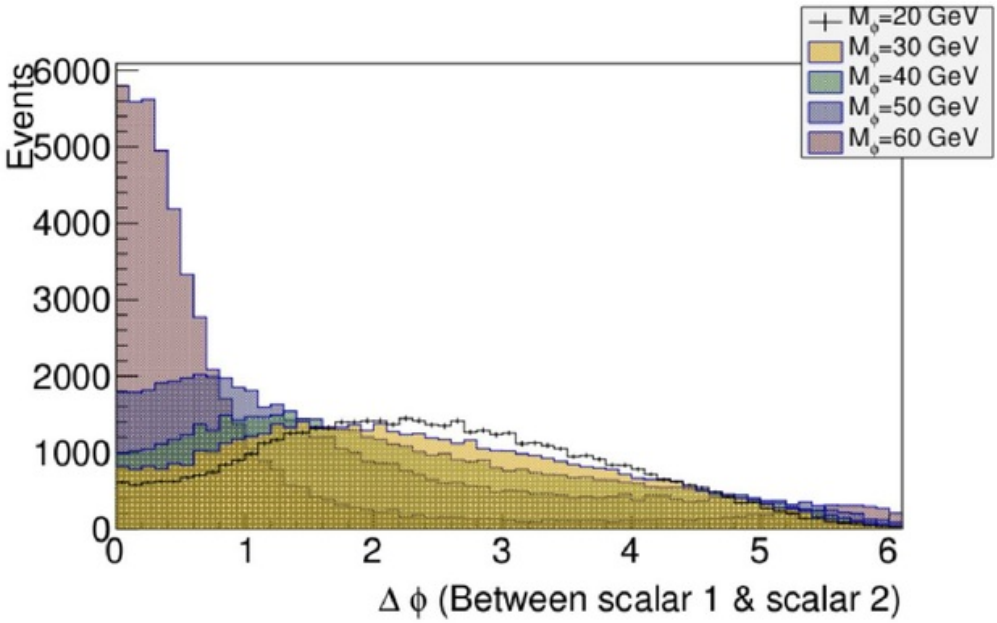

Figure 21: $\Delta\phi$ between each scalar pair for different scalar mass scenarios at the FCChe.

The pair of scalars seem to grow closer together in η and ϕ as the mass increases. Moving forward, the ΔR cut was replaced by a simple $\Delta\eta$ cut. It was discerned that more information is contained in the η distributions, and the $\Delta\phi$ was not as useful of a criterion. For every mass, most of the events have a $\Delta\eta$ of less than 2 between the $b\bar{b}$ pair, which was the cut that was chosen. In addition to this, the further condition that the difference between each scalar ($b\bar{b}$ pair) should also be less than 2. These cuts were justified using Figure's 18 and 20 respectively. An example of the reconstructed dijet scalar masses for the 20 GeV scalar with these cuts can be seen in Figure 22.

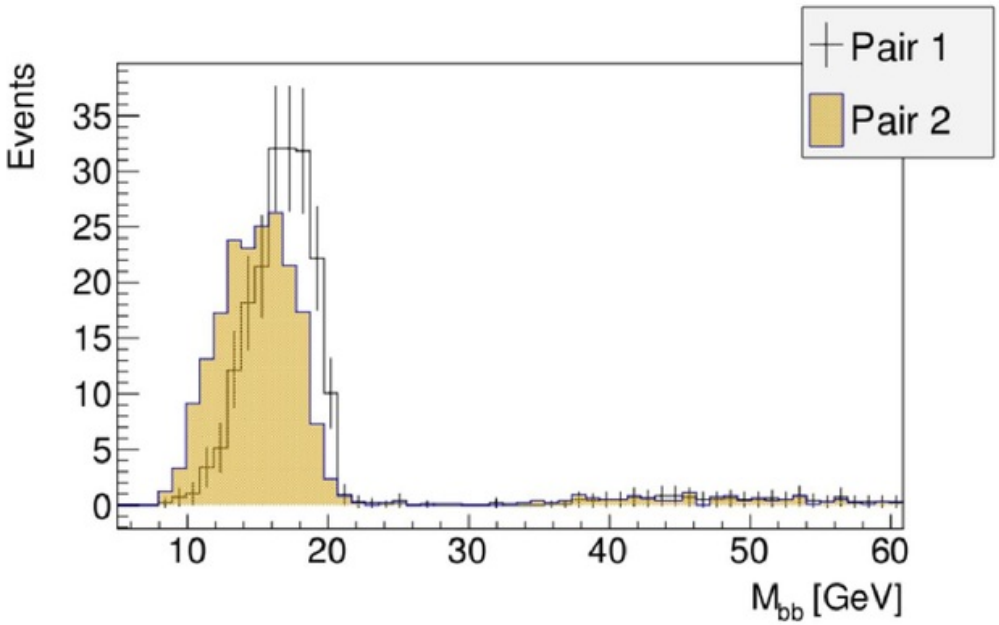

Figure 22: Reconstructed dijet invariant masses using an $\Delta\eta$ cut of $\Delta\eta < 2$, for M_ϕ= 20 GeV at FCChe.

Figure 22 shows good agreement with Figure 14, with slightly more off peak contributions however. This is likely due to the fact that the $\Delta\eta$ cut of 2 is less stringent than a ΔR cut of 2. The 4b distribution is also reconstructed similarly to the method with the ΔR cut, see Figure 23.

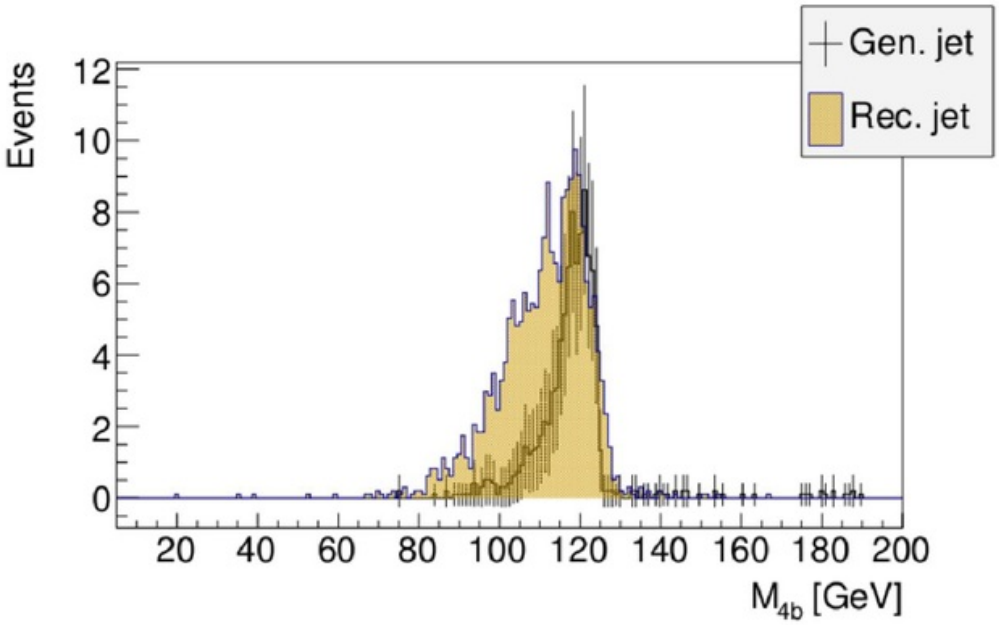

Figure 23: 4b invariant mass distribution obtained using $\Delta\eta < 2$, for for M_ϕ= 20 GeV at FCChe.

Again, the 4b distribution using $\Delta\eta < 2$ is similar to the one obtained using the ΔR cut.

5.4 Anti-kt Study

As mentioned previously, the ΔR separation cut used at the generator level was chosen to be 0.4. The reason for this was that this value was found to be optimal in terms of being able to reconstruct the correct scalar and Higgs masses. With larger jets the issue can be that jet merging can occur. This is a result of the fact that what would be 2 jets with a smaller ΔR cut is now considered as 1, due to a larger ΔR radius. However, the converse issue is faced by having a smaller ΔR cut: small jet fragments resulting from QCD radiation could be interpreted as a real jet when in fact it is not. Figure 24 shows the average mass of the reconstructed jets for different ΔR cut values.

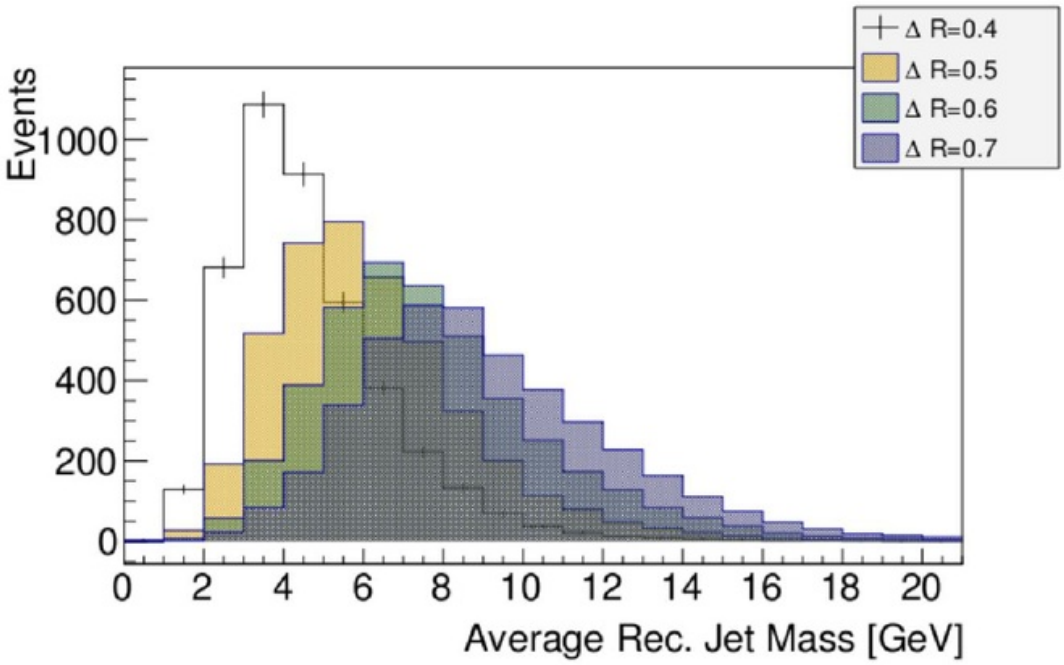

Figure 24: Variation of average reconstructed jet mass with increasing minimum ΔR separation between jets.

Figure 24 shows how the average mass of the jets increases as the ΔR cut is enlarged. The optimal value for accurate reconstruction of the scalar pairs and the Higgs was found to be 0.4. The combinatorics method with the other ΔR options either returned incorrect mass peaks, or were unable to operate as the jet conditions were not met: for instance it is required that there are 4 distinct jets, close in mass and ΔR, and therefore if the jets are merged it may not be possible to form 2 distinct pairs made of 2 jets with similar masses etc. Due to this, the conditions were not met so scalar reconstruction could not take place. This was the basis for using a value of 0.4 throughout the study.

6 Detector-level Studies for Background Processes

6.1 4b Final State

As discussed, many standard model processes have a 4b final state and there is also the additional issue of jet mistagging. Typical b-tagging efficiencies are around 70% identification, while mistagging efficiencies are typically in the range of 10%. For this reason, processes that do not necessarily have a 4b final state must be considered, as other light jets may be wrongly interpreted as b's.

The main background samples that were generated are outlined in Table 5.

Sample	Process	Generator Level Constraints	Cross Section (fb)
Signal[1]	h→φφ→b b~ b b~	PT of Jets/b's/photons/charged leptons > 6.5 GeV η of Jets/b's/photons/charged leptons < 6.1 Min. ΔR between jets = 0.2 Min. Inv. Mass of Jet/bb~ pair = 8 GeV	51.34
CC Single Top Production	pe-→j t~ vl all /h (t~ → W- b~, W- → all all	PT of Jets/b's/photons/charged leptons > 6.5 GeV η of Jets/b's/photons/charged leptons < 6.1 Min. ΔR between jets = 0.2 Min. Inv. Mass of Jet/bb~ pair = 8 GeV Beam Polarisation = -80%	11,347
CC Top+Multijet Sample	all = g u c d s u~ c~ d~ s~ , ve vm vt ve~ vm~ vt~ ta- ta+ b b, ~ z w+ w- h t t~ pe- → b~ all all vl pe- → b all all vl	PT of Jets/b's/photons/charged leptons > 6.5 GeV η of Jets/b's/photons/charged leptons < 6.1 Min. ΔR between jets = 0.2 Min. Inv. Mass of Jet/bb~ pair = 8 GeV Beam Polarisation = 0	9683
CC Inclusive Single W/Z/h Production	p e- → vl w- j j / t~ t , w- → j j p e- → vl h j j , h → j j p e- → vl z j j , z → j j	PT of Jets/b's/photons/charged leptons > 6.5 GeV η of Jets/b's/photons/charged leptons < 6.1 Min. ΔR between jets = 0.2 Min. Inv. Mass of Jet/bb~ pair = 8 GeV Beam Polarisation = 0	3566
CC b b~ + 2j Production	all = g u c d s u~ c~ d~ s~ ve vm vt ve~ vm~ vt~ ta- ta+ b b~ p e- > b~ b all all vl	PT of Jets/b's/photons/charged leptons > 6.5 GeV η of Jets/b's/photons/charged leptons < 6.1 Min. ΔR between jets = 0.2 Min. Inv. Mass of Jet/bb~ pair = 8 GeV Beam Polarisation = 0	1120

Table 5: List of the main background samples that were produced, in addition to the signal sample[1], with the process, generator level cuts and cross section.

Examples of some processes with 4b final states can be seen in Figure 25.

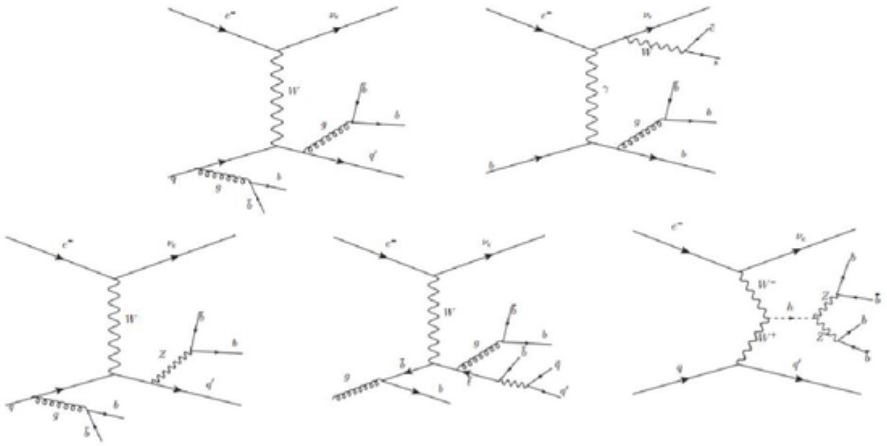

Figure 25: Feynmann diagrams outlining some of the main background processes contributing to a 4b final state. (Source: S. Liu et al, Exotic Higgs Decay $h \to \phi\phi \to 4b$ [35].)

The main background that is particularly large is the t+jets, with the cross section for this process at FFChe being 11,347.65 fb, while the signal cross section is around 51.34 fb. The single top production includes polarisation however, while all the other samples do not. Polarisation is related to the number of spin up and spin down particles,

$$P = \frac{N_+ - N_-}{N_+ + N_-}. \tag{16}$$

The effect of beam polarisation is simply to multiply the cross section by (100-P)/100, 1.8 in this case. So to counteract this the other backgrounds and signal must be scaled to give a proper comparison. The top+multijet background sample provides an alternative method to the top background by letting Pythia decay the particles and not Madgraph. By letting Pythia handle the decays, this sample is also inclusive of other multijet signatures, not just the top quark decaying into a b and a W. This therefore gives a more realistic background sample, but as the top background is the most dominant sole process, it was still useful for later stages of analysis. Another important background sample is the inclusive W/Z/h sample. This sample includes all W/Z/h decays into all jets, and was another source of 4b final state events. Charged current $t\bar{t}$ production was also considered, but it was found that the cross section was negligibly small in comparison to the other background samples (7.45 fb).

Another source of $t\bar{t}$ background events, which can be a significant source of 4b production, is photoprodution. Photoproduction occurs when the momentum exchanged between two particles (i.e. the photon energy) is large enough such that pair production can occur, in this case of a $t\bar{t}$ pair. Photoproduction events are typically characterised by a forward deflected electron (shallow angles of around a degree). These electrons can be detected by a forward calorimeter, which then acts as an electron tagger of sorts, allowing the identification/elimination of photoproduction

events [37]. The calorimeter is a detector which measures the energy lost by a particle in a section of silicon. As hadrons fragment and hadronize, they will shower sooner in the calorimeter than say electrons; allowing the identification of forward electrons by characterizing the measured showers, i.e. electromagnetic vs. hadronic showers [38]. For this reason (assuming photoproduction events can be identified and discarded), photoproduction was not considered as a background process in this study.

6.2 b-tagging Requirements

As discussed, the b-tagging efficiency is an important factor in the model/simulation as it reduces the number of true b tagged jets, while also falsely identifying non b jets as b jets. A naive estimate at the level of signal lost would be proportional to the efficiency to the power of the number of required btagged jets. For example 4 jets requiring a b-tag, with a b-tagging efficiency of 70%, would give an overall efficiency of 0.70^4 (24%).

For this reason, methods were explored with differing numbers of required b-tagged jets, as this would increase the efficiency. The explored requirement options were: no b-tag requirement, 1 b-tag in each reconstructed scalar pair (2 out of 4 jets b-tagged) and finally all 4 jets b-tagged. It was found that even without b-tagging, and using the method of combinatorics, that the scalar and Higgs masses could be reconstructed quite accurately. The problem occurred however that with no b-tagging requirement, the top background was substantially large. Even with 2 b-tags the top background alone was such that the signal cross section was much too small to be observed.

Examples of the scalar/Higgs reconstruction, for the signal (20 GeV scalar), using no b-tag requirement and 1 b-tag in each scalar pair can be seen in Figure's 26 and 27.

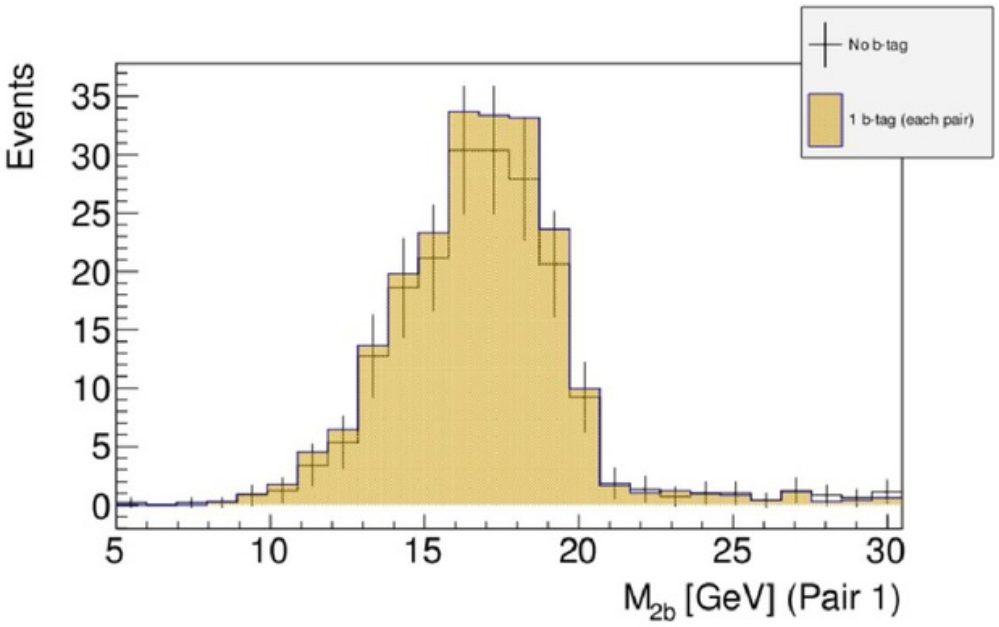

Figure 26: Scalar pair 1 (20 GeV) reconstruction using no and 1 b-tag requirement at FCChe. Corresponding pair 2 plot can be seen in Figure 53 in the Appendix.

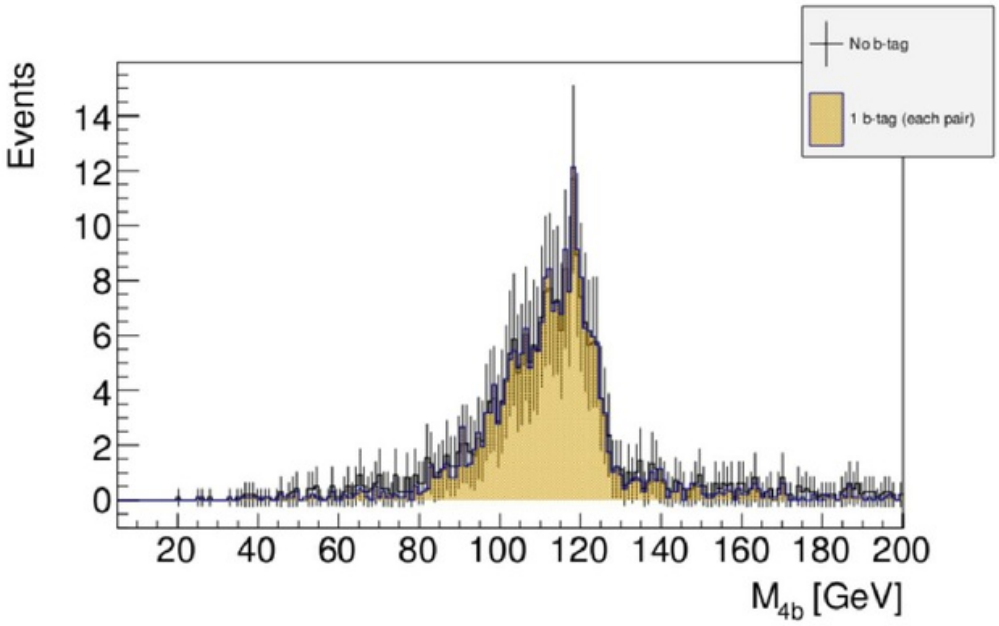

Figure 27: Higgs reconstruction using no and 1 b-tag requirement for the 20 GeV scalar at FCChe.

Both distributions show very similar results, although it should be remembered that the distribution with no b-tag requirement is inclusive of the 1 b-tag distribution. These plots show how

even considering no b-tag requirement or only 2 b-tags, the scalar pairs, and subsequently the Higgs, can be reconstructed well. However, simply considering the top quark background alone shows why this strategy could become problematic. The backgrounds using this method were so large that it would be difficult to discern a signal. Figure's 26 and 27 show the top background plots for the scalar and for the Higgs corresponding to no b-tag requirement and 1 b-tag requirement.

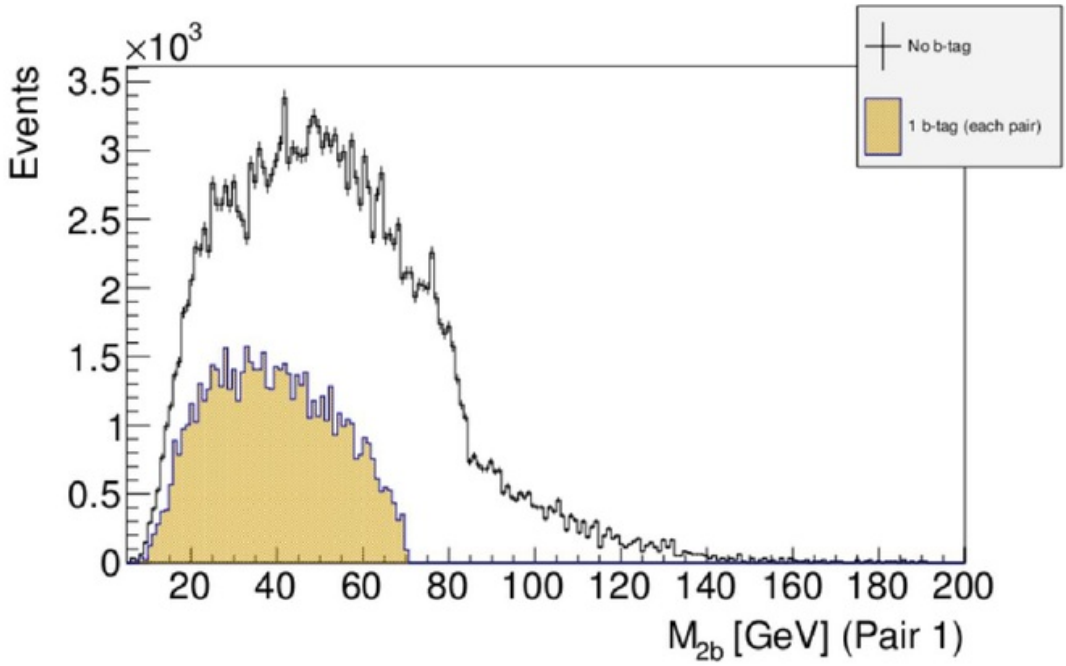

Figure 28: Dijet mass for top+multijet backgrond with both; no b-tag requirement and 1 b-tagged jet per dijet at FCChe. For the corresponding plot for pair 2, see Figure 54 in the Appendix.

From Figure 28, it is clear that a significant number of top quark background events pass the criteria with both 1 and no b-tagging requirement; much more than the signal process.

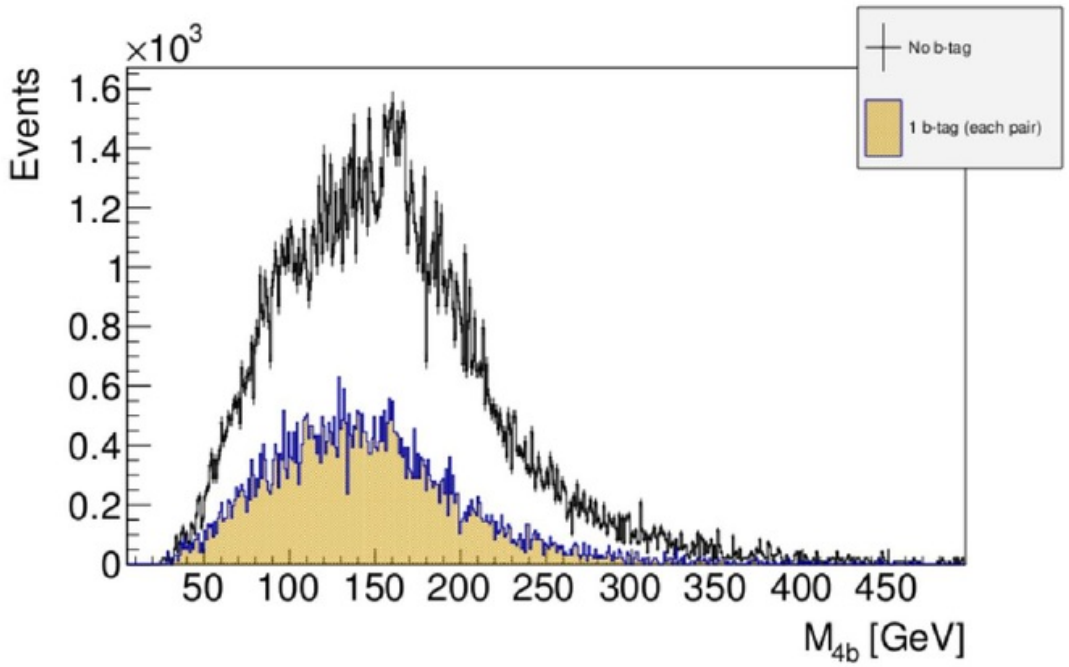

Figure 29: 4b invariant mass distribution wih no b-tagging requirement and 2 b-tagged jets, for the top+multijet background at FCChe.

In the final analysis it was therefore decided that all 4 jets should require a b-tag. This gave the best signal to background ratio as it removed a significant number of top background events. Clearly higher b-tagging requirements will also remove many signal events, but a much higher proportion of background events were killed, as will be discussed in the next section. However, this analysis was performed still assuming a b-tagging efficiency of 100%, and a misidentification rate of 0%. An exploration of more realistic b-tagging scenarios will be given in Section 7.4.

7 Results

7.1 Sensitivity to Pseudorapidity Range

For the final analysis, an η cut of $\eta < 2.5$ for the jets was chosen. The basis for this cut was the significant reduction in background events, compared to a less severe loss of signal events. This strategy also follows from the analysis strategy used at ATLAS in a similar search [23]. Figure's 30 and 31 show the cut flow in η for the signal and top background respectively; for 4-jets with no b-tagging requirement.

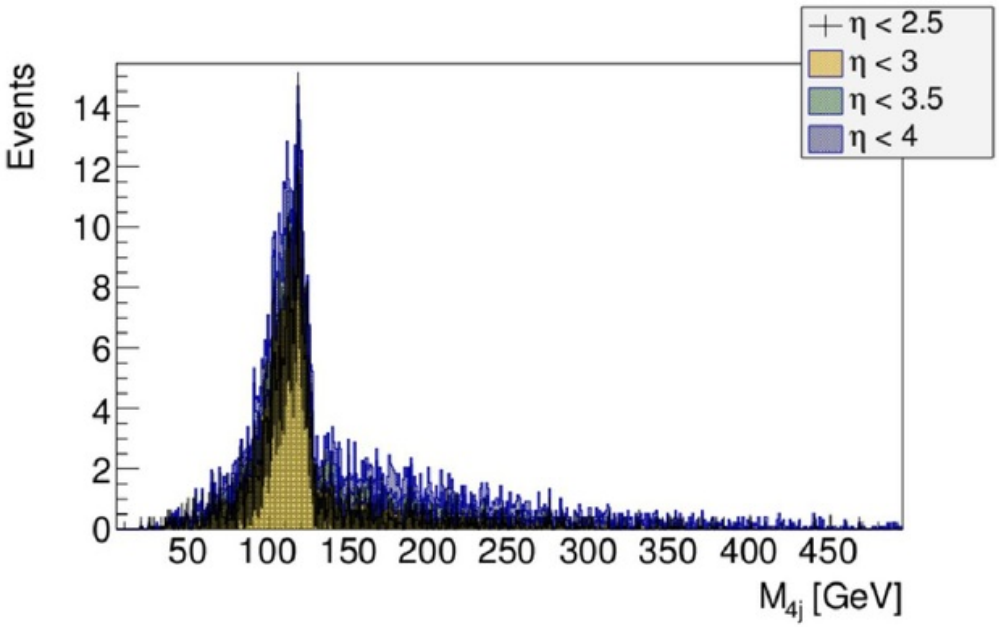

Figure 30: 4-jet cut flow for 20 GeV scalar (with a PT cut of 8 GeV in place which will be explained in the next section).

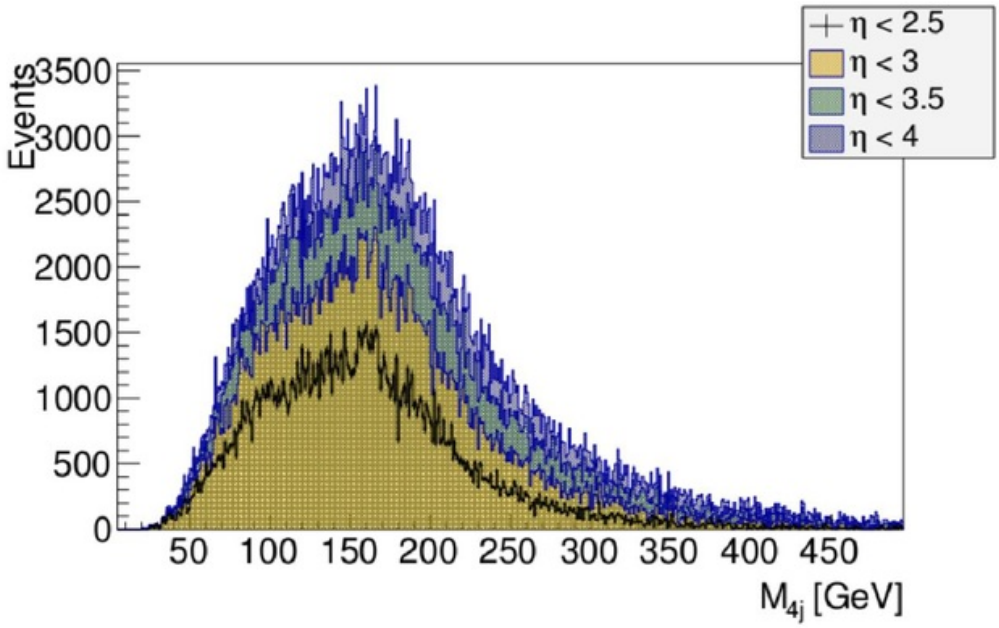

Figure 31: 4-jet cut flow for top background, again with 8 GeV PT cut in place (with polarisation of -80%).

Clearly from these figures, the effect of the η cut is more pronounced for the top background than it is for the signal process. Table 6 shows the number of events with 4 b-tags, for each of the cuts, for the 20 GeV scalar and the top background.

	Events [4b peak 100-140 GeV]		
η Cut	20 GeV Scalar	Top Background	Sig/Back
4	296	494	0.60
3.5	270	397	0.68
3	232	276	0.84
2.5	183	178	1.03

Table 6: η cut flow for 20 GeV scalar and dominant top background (b-tagging efficiency 100%, at FCChe).

$\eta < 2.5$ is the only cut with a signal to background ratio greater than 1. Also note that the number of events for the top background has been divided by 1.8, due to beam polarisation for this sample.

7.2 Sensitivity to Minimum Transverse Momentum

The effect of different PT cuts on both the signal, and the dominant top background was also investigated. The purpose of doing this study is to find the optimal cut that gives the best signal to background ratio. Other considerations that must be made are the effects of small radiative QCD jets and also the mass of the particle being considered. Complications arise when the PT cut is of the order of the particle mass, as many events will not pass the cut. Figure 32 shows the cut flow of the signal with a range of different PT cuts, while Figure 33 shows the same cut flow for the top background sample; both for 4-jets with no b-tagging requirement.

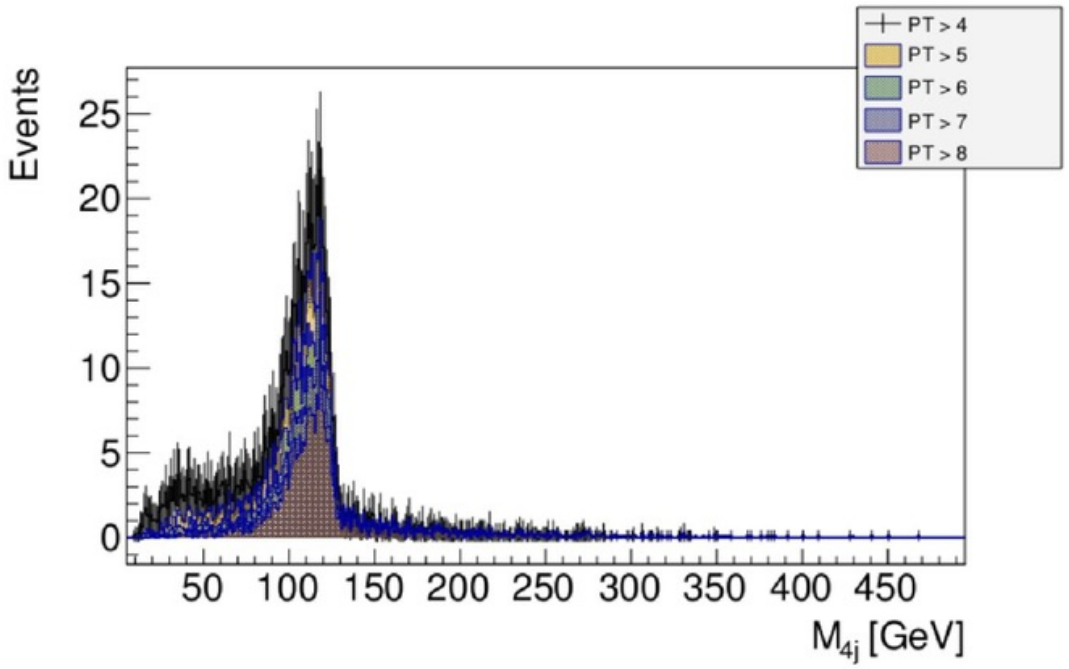

Figure 32: PT cut flow for the 20 GeV scalar.

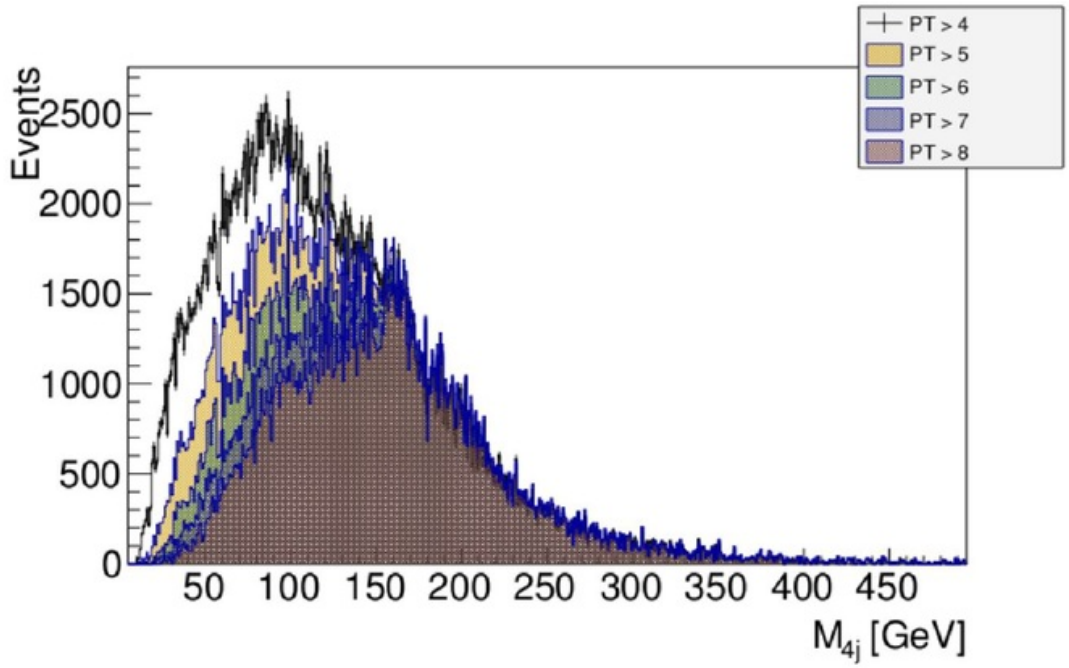

Figure 33: PT cut flow for the top background (with polarisation of -80%).

Table 7 shows the number of events in a broad Higgs mass window with all 4 jets b-tagged. This illustrates the correlated effect on the signal and the background.

	Events [4b peak 100-140 GeV]		
PT Cut [GeV]	20 GeV Scalar	Top Background	Sig/Back
4	451	460	0.98
5	371	351	1.06
6	296	293	1.01
7	237	259	0.92
8	183	178	1.03

Table 7: Note that the values displayed here for the top background are divided by a factor of 1.8 as they were produced with a beam polarisation of -80%.

Even though the PT cut of 5 provides a higher signal to background ratio, the final cut that was chosen was of 8 GeV. This was because lower PT cuts give small proto-jets the opportunity to be considered, increasing the number of wrongly reconstructed scalar pairs. However, as a rule of thumb the PT cut should not be greater than approximately half the mass of he particle (10 GeV in this case). That is why this study was performed with the 20 GeV scalar, as this is the most sensitive signal to the cut. A PT cut of 8 is on the boundary of what is acceptable for this mass of scalar.

7.3 Dijet Mass Binning

Another cut that was imposed on the samples was that each dijet pair should lie inside the same mass window, e.g. if one dijet has a mass of 10 GeV, but the other has a mass of 40 GeV, the event will not be considered. The mass bins that were used were 10-20 GeV, 20-30 GeV, 30-40 GeV, 40-50 GeV and 50-60 GeV. So in an event, both dijets must have a mass in the same bin for the 4-jet mass to be reconstructed. This gives a method to obtain the rough mass range that the scalar lies in, i.e. if a Higgs peak is observed in the 4b distribution for a certain mass window, we can constrain the scalar mass to lie within this range, even if the dijet peak is drowned in background events (as was the case).

It was found however that this method was not as effective for the heavier (50/60 GeV) scalars, due to the fact that they had broad dijet peaks (the dijets cover a larger mass range and do not necessarily share near equal masses, therefore the dijets do not fall into the same mass bin). For the 20 GeV sample for example, most of the events should occur in the 10-20 GeV bin, and the counts in the other bins should be a small random fluctuations. Whereas for the heavier scalars, the counts were distributed across the bins almost equally, with no excess in the bin corresponding to the scalar mass in question. Figure's 34 and 35 show the dijet masses for the 20 and 60 GeV scalars, illustrating the broad dijets observed for the heavier masses.

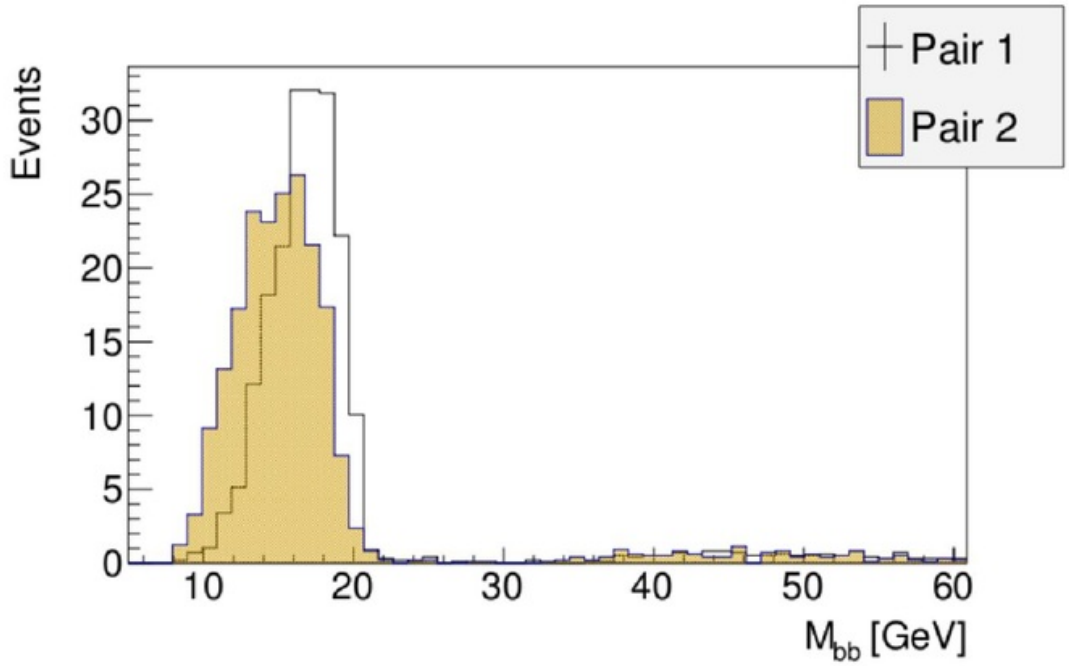

Figure 34: The dijet peaks for the 20 GeV scalar are relatively narrow and have a shoulder close to 20 GeV, however pair 2 is shifted to slightly lower masses.

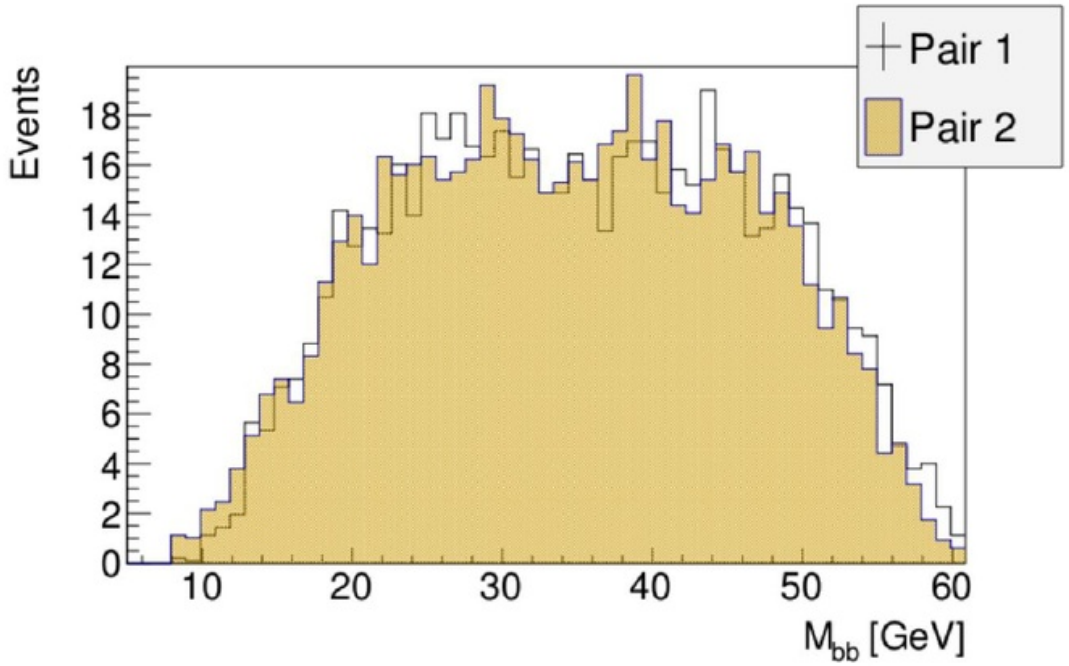

Figure 35: 60 GeV reconstructed dijets with both dijets containing 2 b's.

The dijets for the 60 GeV scalar are much broader and cover the whole range of masses below 60 GeV, with no sharp shoulder at 60 GeV, however the peak does tail off at 60 GeV. An example of how the 4b signal behaves in the 10-20 GeV mass bin for the 20 GeV scalar can be seen in Figure 36.

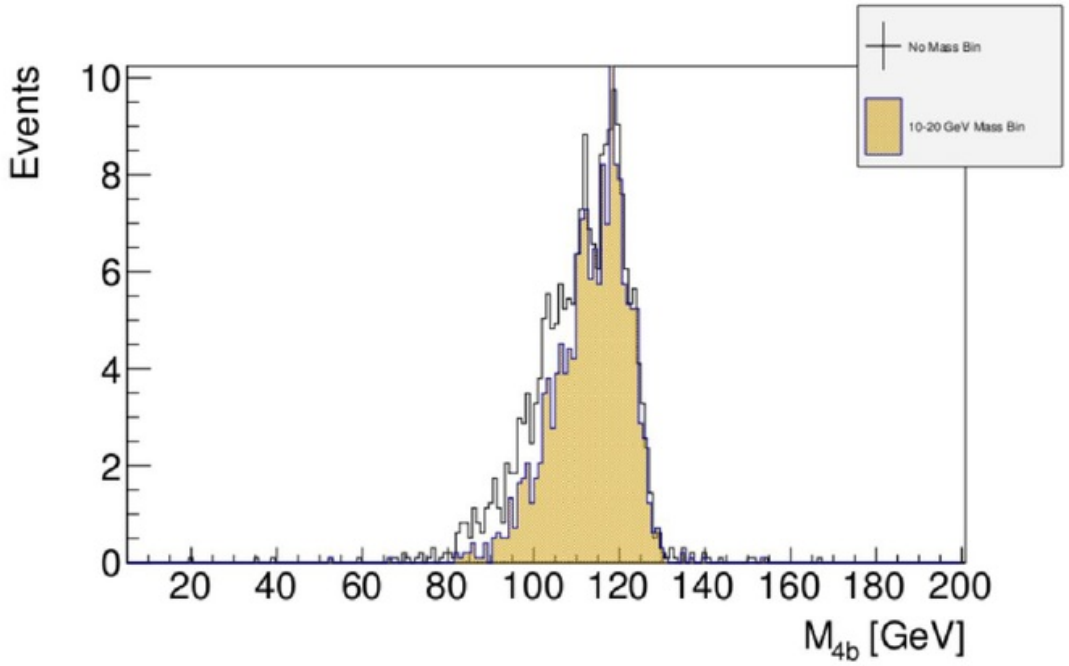

Figure 36: The Higgs peak is reconstructed well using the 10-20 GeV mass bin for the 20 GeV scalar; with the 50-60 GeV bin and the 60 GeV scalar the reconstruction isn't so well defined (result of Figure 35).

The 4b peak reconstructed using the mass bins follows the peak with no mass bin requirement closely, with some reduction in statistics; 148 events with the mass bins and 183 events without. However, as will be discussed, the corresponding reduction in top background events is much more considerable. These figures are with 100% b-tagging efficiency and 0% mistagging however.

7.4 Effect of b-tagging Efficiency

As discussed in the previous b-tagging efficiency section, a study with more realistic b-tagging efficiencies was performed. In this study, the b-tagging efficiency was set to 70%, with a mistagging efficiency of around 10%. Mistagging means that light jets will be wrongly considered as b's. Figure's 37 and 38 show the 100% b-tagging scenario vs. the more realistic b-tagging set up for the signal and top background respectively.

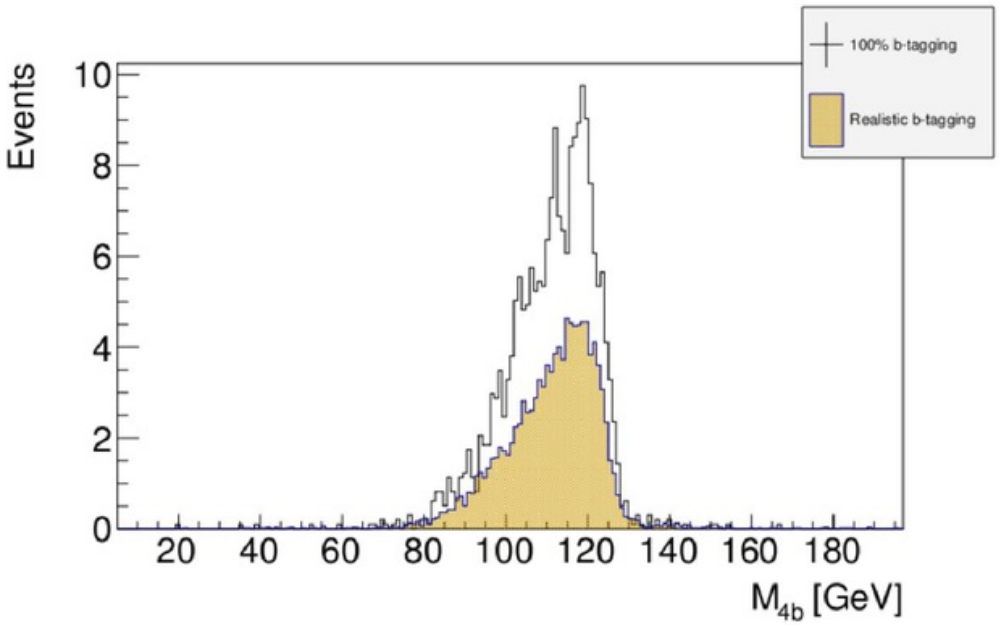

Figure 37: 20 GeV scalar 100% and realistic b-tagging 4b distribution. A similar trend is seen in the dijet peaks (Figure's 58 and 59 in the Appendix).

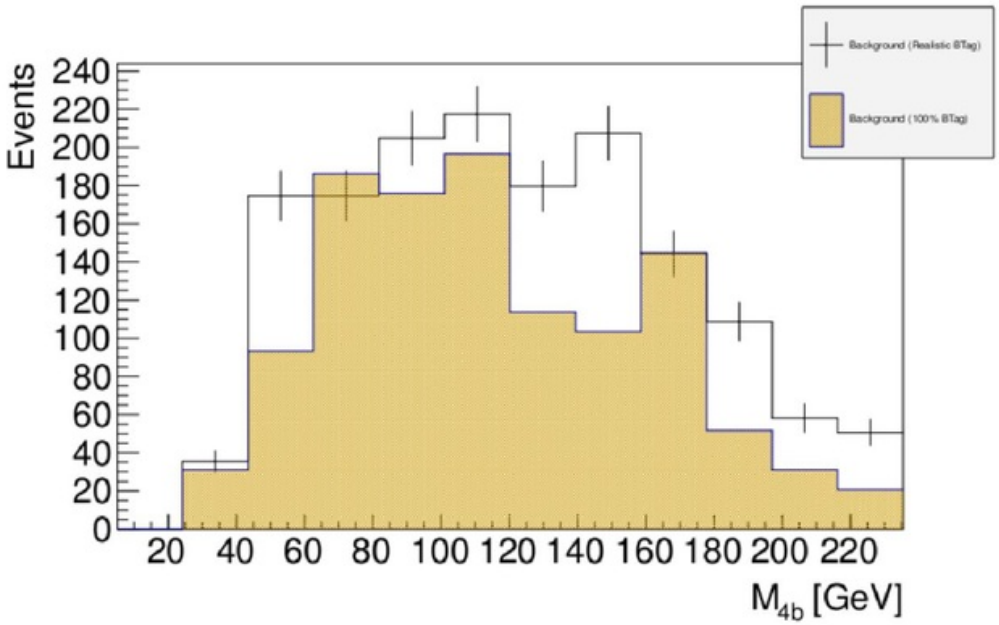

Figure 38: Here an increase in b's identified is observed. This is likely a result of the misidentification of light jets.

Table 8 shows the ratios of the realistic b-tagging events in the Higgs mass window, to the 100%

events for the 20 GeV scalar with the cuts outlined in the previous sections.

	Events [4b 100-140 GeV]		
Scalar Mass [GeV]	100% BTag	Realistic BTag	Real/100%
20	183	100	0.55
30	300	167	0.56
40	237	137	0.58
50	218	131	0.60
60	239	146	0.61

Table 8: The efficiency is around 50-60%, increasing towards higher masses, which may be attributed to the broader dijet peaks.

The observed efficiencies are in the range of 50-60%, which is much better than the naive estimate of 0.7^4 (24%). The fact that light jets may be misidentified as b's should also be salient however, as this will increase the number of observed b's.

7.5 Initial Signal to Background Comparison

A first estimate of the observed signal was made via comparison of the signal to the background with realistic b-tagging and all the outlined cuts in place. For this section of analysis, for illustrative purposes, the signal is compared to the top+multijet background sample (as it is orders of magnitudes larger than the other backgrounds). The cut flows and constraints were worked out using the top background sample, as this is by far the dominant sample; but for this analysis, as it is more comprehensive, the top+multijet sample was used. Figures 39 to 41 show the signal to background for the 20, 30 and 40 GeV scalar in their respective mass bin windows. In this section, both signal and background samples are unpolarised.

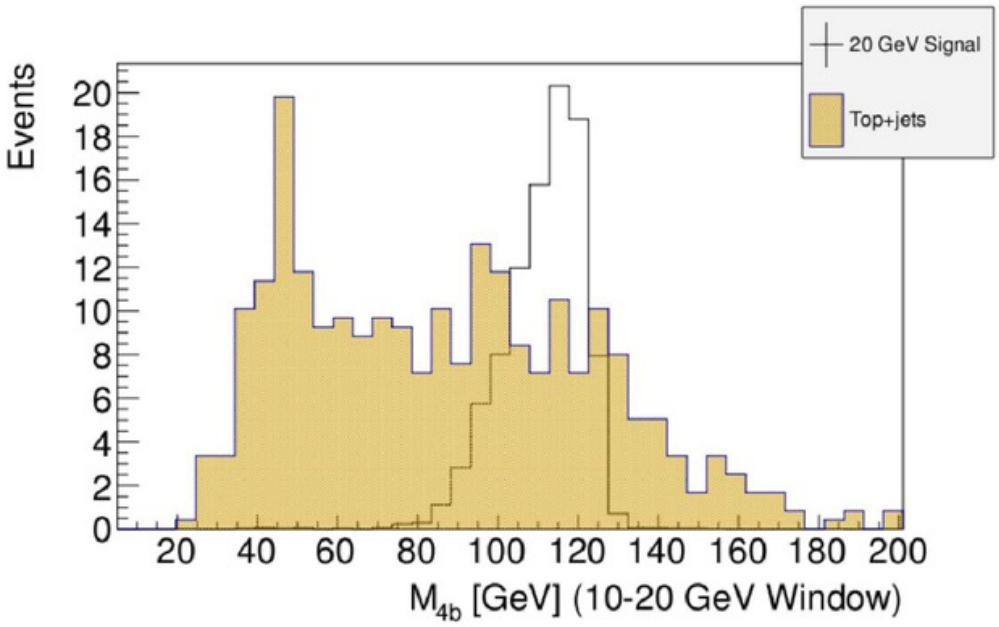

Figure 39: Signal to background for 20 GeV scalar and top+multijet background in the mass bin range of 10-20 GeV.

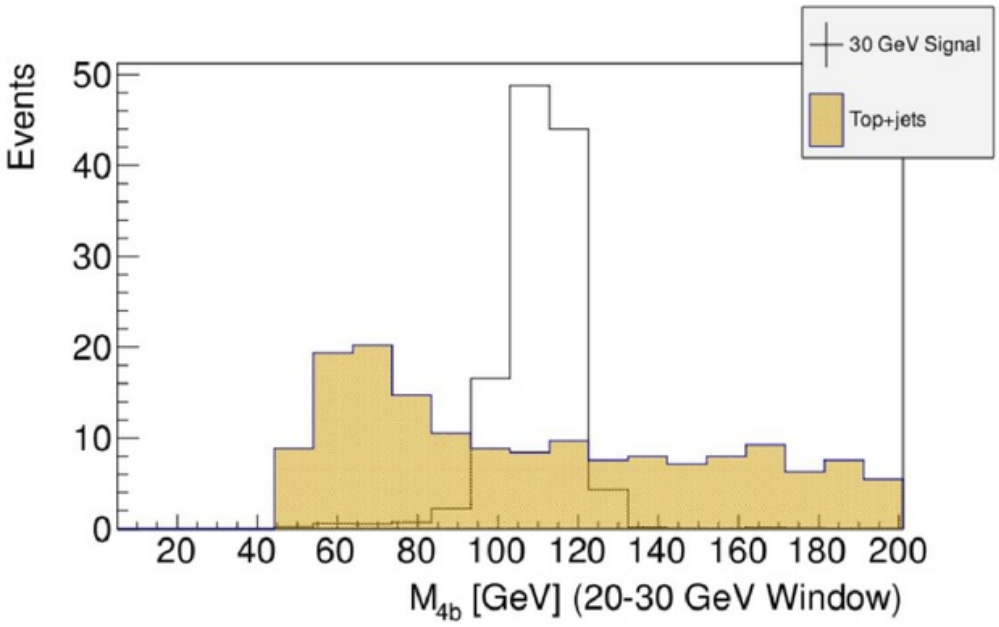

Figure 40: Signal to background for 30 GeV scalar and top+multijet background in the mass bin range of 20-30 GeV.

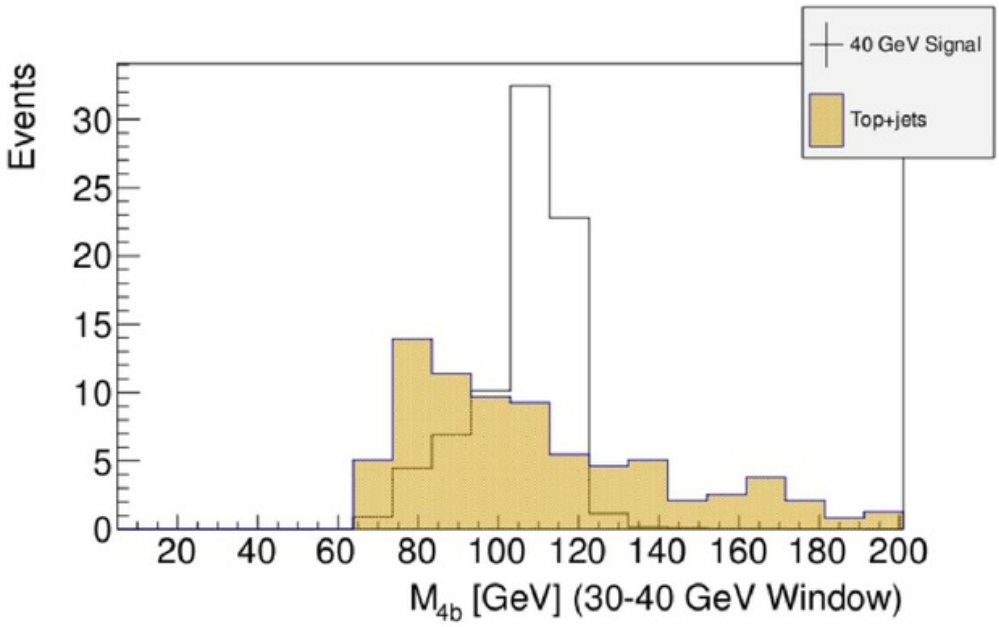

Figure 41: Signal to background for 40 GeV scalar and top+multijet background in the mass bin range of 40-50 GeV.

This technique was successful for these masses, as each resonance is clearly visible over the background in the same mass bin range; but as discussed, the mass window method was ineffective for the 50 and 60 GeV scalars. This was due to their broad scalar resonance width. Figures 42 and 43 show the 4b signals for the 50 and 60 GeV scalars without mass window conditions, compared to the top+multijet background sample. These figures illustrate that these signals are unobservable, and as the mass window method could not be utilised again, the 50 and 60 GeV signals could not be observed.

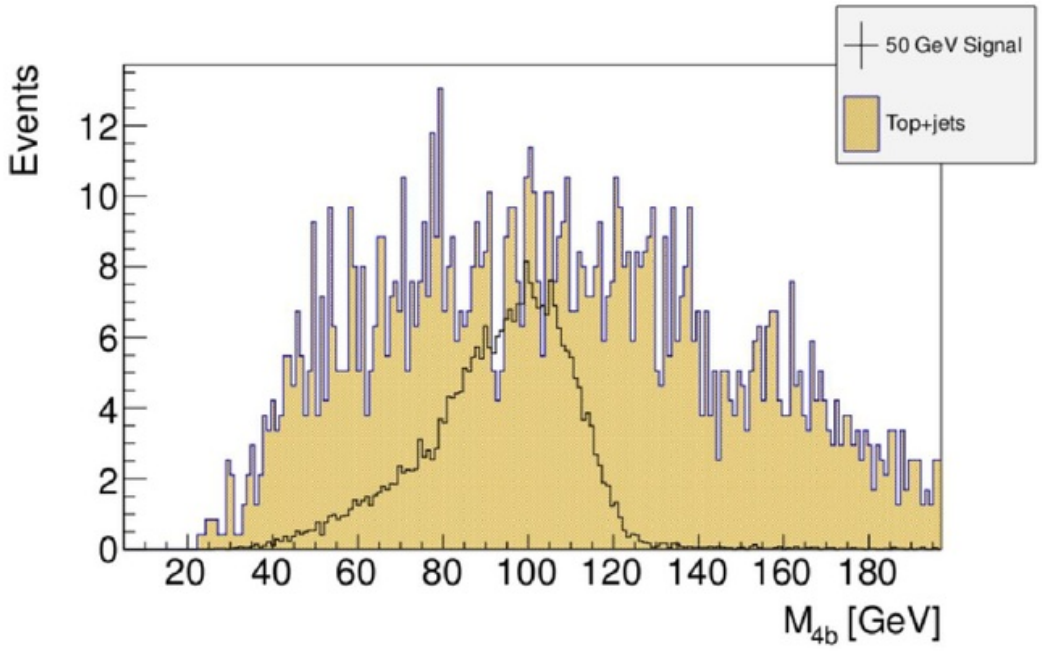

Figure 42: Signal to background for 50 GeV scalar and top+multijet background with no mass bin requirements.

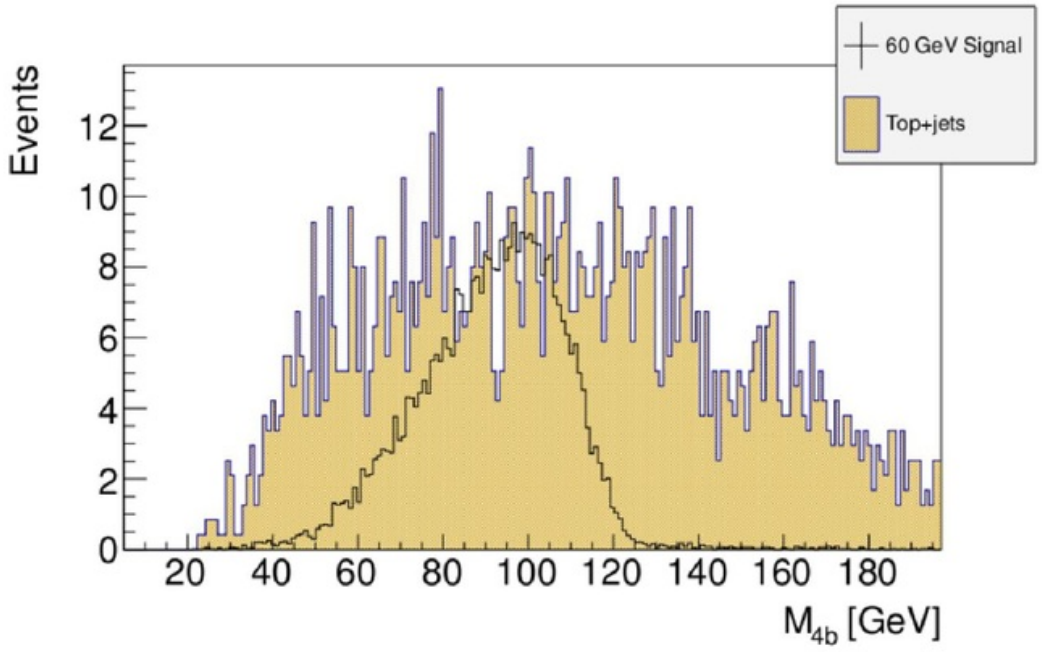

Figure 43: Signal to background for 60 GeV scalar and top+multijet background with no mass bin requirements.

Figures 42 and 43 show that the background without scalar mass binning is much more sizeable than with binning. The 50 GeV signal is completely swamped by background events, and while the 60 GeV peak is slightly visible, with more comprehensive backgrounds this would not be enough to classify the signal. As will be illustrated in the next section however, further analysis techniques can be exploited (namely TMVA), even if the signal is swamped completely by background. This first impression of the signal to background ratio would likely be further diminished by other unconsidered background events and more sophisticated techniques would certainly be required, even for the lower mass scalars which display resonances here.

7.6 Boosted Decision Tree Analysis

As alluded to, another analysis strategy that can be explored is the use of Boosted Decision Tress (BDT) using the Toolkit for Multivariate Data Analysis (TMVA) [39]. Boosted decision trees are used to split data into signal like events, and background like events, by using a Monte-Carlo simulation of both signal and background events, to train the decision tree [40]. This gives the tree information on how the signal and background topologies differ, for given variables chosen. The important aspect is to choose variables that are significantly different enough between signal and background, so that events can be separated accordingly. Once the tree has been trained, the final samples can be tested and classified. BDT is a method that is used extensively in high energy physics, and has been utilised in many standard model Higgs searches before [41, 42].

So even if the signal is completely swamped by background events, BDT can be used to exploit differences in the topologies of the signal and background, identifying whether an event is signal or background like. This is the main power/benefit of BDT analysis; even if the signal is lost to background, as long as they have distinct topologies, a signal can be discerned from the background. The initial sample of events (node) is split up into branches, based on whether an event seems signal or background like (in comparison to the training sample used to train the tree). Once the sample cannot be split further, there will then be a number of terminal nodes (leaves), which represent signal like, or background like events. This is how one can determine signal from background events using BDT analysis.

Boosting is used to increase the weight given to misclassified events (signal events classified as background or background events classified as signal). A second tree is then made with the new weights, and the same process is repeated iteratively. Then after passing through multiple trees, if an event lands on a signal leaf it gets a score of 1 and if it lands on a background leaf, it gets a score of -1. Therefore a high score means a sample is signal like, and a low score means a sample is background like. A common boosting algorithm used to do this is the AdaBoost algorithm [43]. However a consideration when using BDT analysis is overtraining. This is when the tree learns statistical fluctuations, and uses them to wrongly classify whether an event is signal or background like [39].

Some examples of variables that could be used for BDT analysis are the $\Delta\eta$ between the jets

in each dijet, the $\Delta\phi$ between the jets in each dijet and the HT variable for each event. The HT variable is the linear sum of the transverse momentum (PT) of all jets in a given event [44]. Figures 44 to 46 show all of these variables respectively, for the 60 GeV signal and the top+multijet background sample. These distributions are normalised to illustrate the topological differences between the signal sample and the background sample.

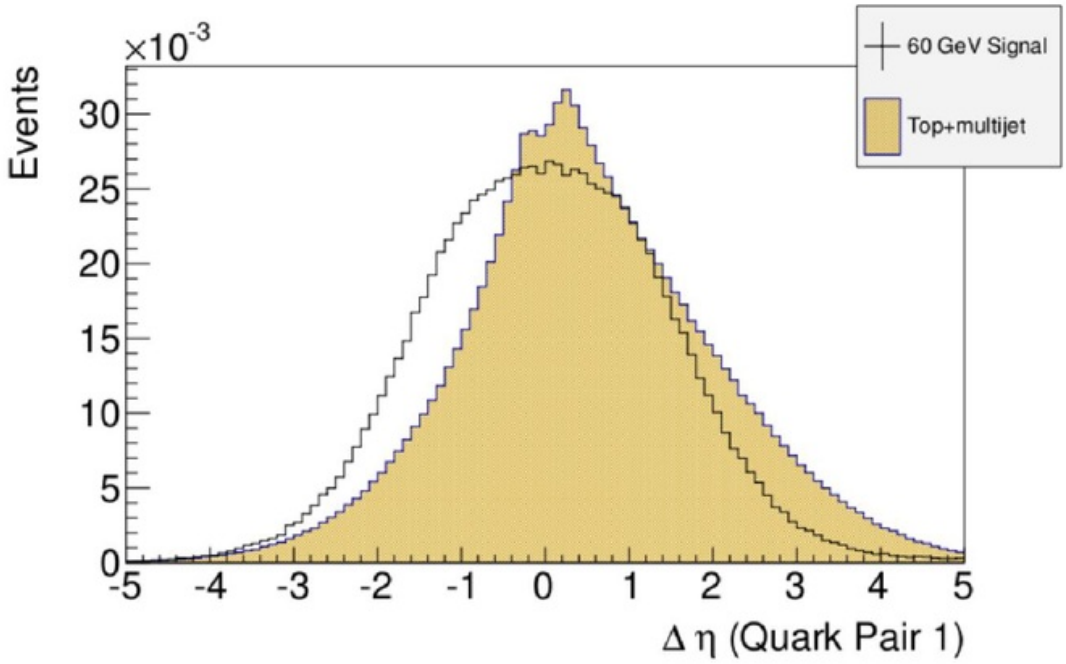

Figure 44: $\Delta\eta$ between each quark in the first dijet pair.

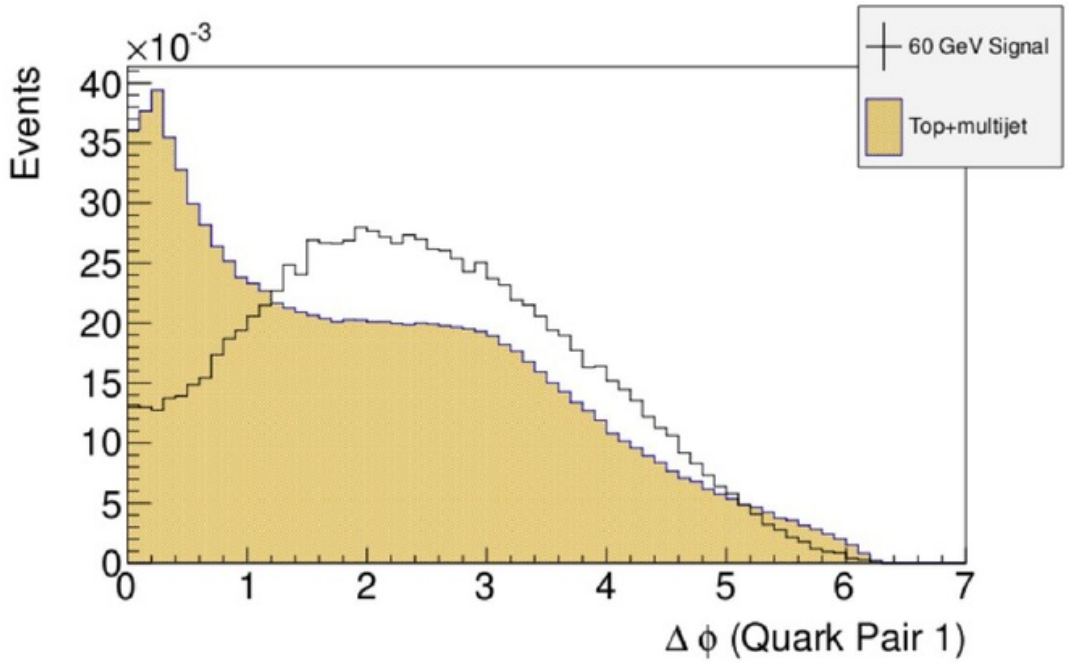

Figure 45: $\Delta\phi$ between each quark in the first dijet pair.

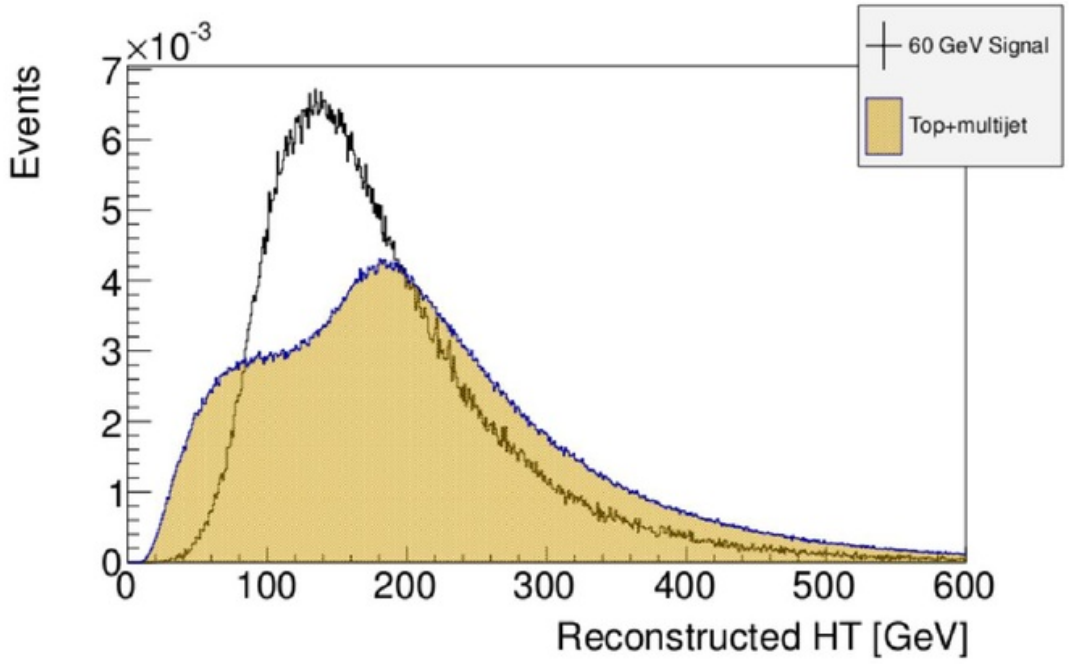

Figure 46: Scalar sum of all jet PT (HT).

A small BDT of 7 variables was applied to each of the signals in turn, with the top+multijet

background, in addition to the W/Z/h+multijet backgrounds outlined in Table 5. The 7 variables that were used in the BDT were: the difference in mass of the 4 first highest PT jets and the 3 first highest PT jets, the invariant mass of the 4 jets chosen through the method of combinatorics, the difference in mass between the two scalar candidates, the missing energy, the number of reconstructed jets, the reconstructed HT and finally the difference in the ΔR between the two scalar candidates. Additionally, all events passed to the BDT were required to have 4 b-tagged jets, then as described, the tree was first trained, and then used to classify the signal.

Figures 47 and 48 display the BDT probability outputs for the 20 and 60 GeV scalar with, as discussed, the top+multijet and W/Z/h+jets background samples.

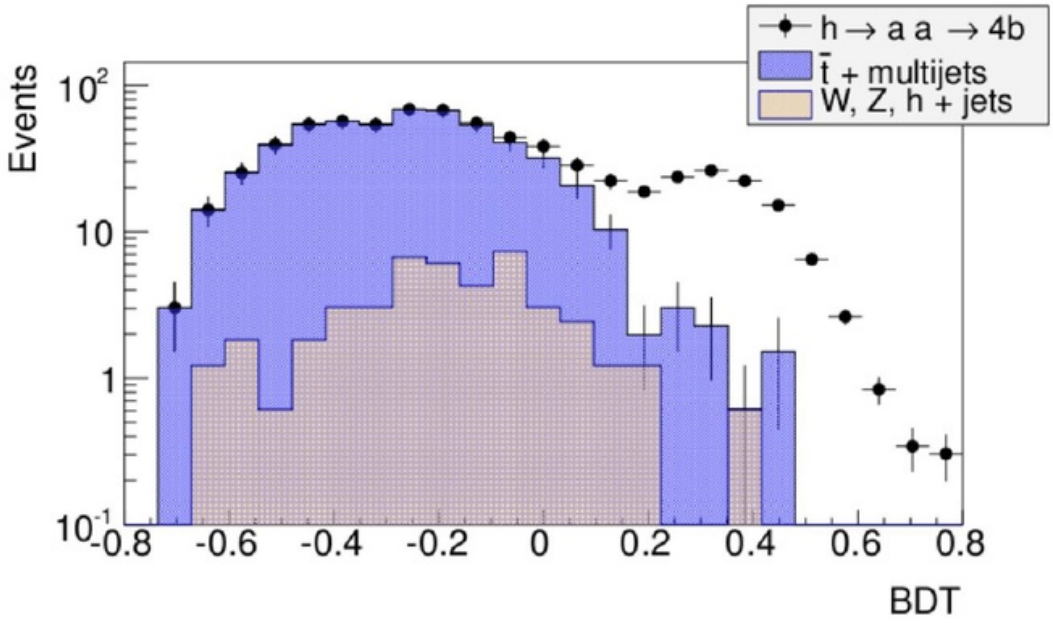

Figure 47: BDT output for the 20 GeV scalar (a) sample, trained with the 7 variables discussed.

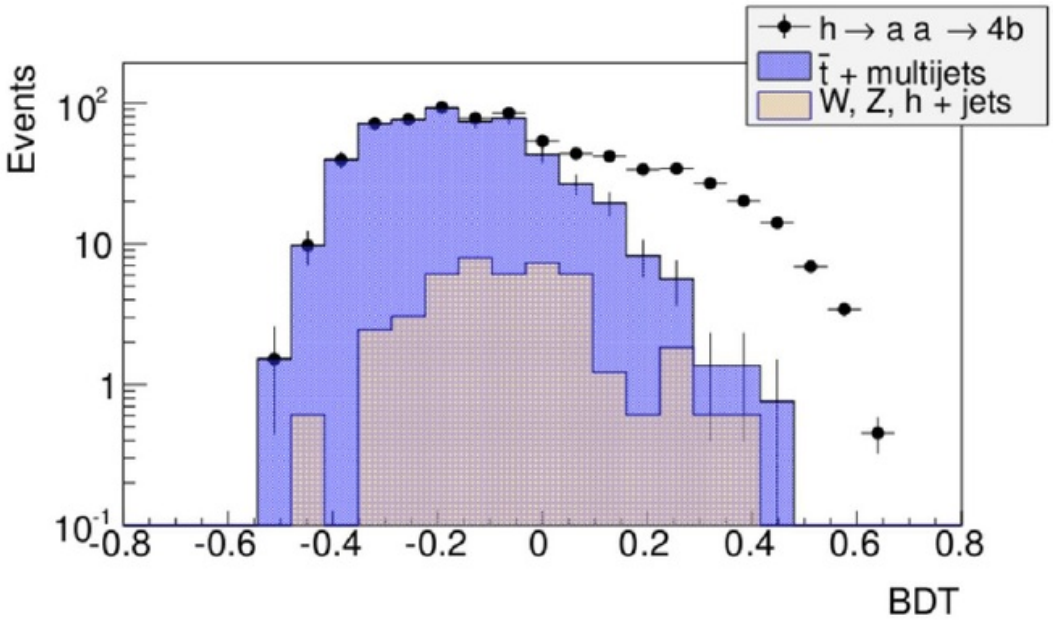

Figure 48: Corresponding BDT output for the 60 GeV scalar (a) sample.

These figures show the effectiveness of BDT analysis, i.e. identifying background events as background events and signal events as signal events. A negative score means a background like event, while a positive score means a signal like event. Therefore it was decided to perform BDT cut of > 0, as above zero the signals and backgrounds can be discerned with much success.

7.7 Signal to Background Comparison Using Multivariate Analysis

Figures 49 and 50 show the reconstructed 4b invariant mass distributions with the cut of BDT > 0. This cut was chosen as a conservative baseline to see what kind of results can be obtained with the chosen variables in the BDT method.

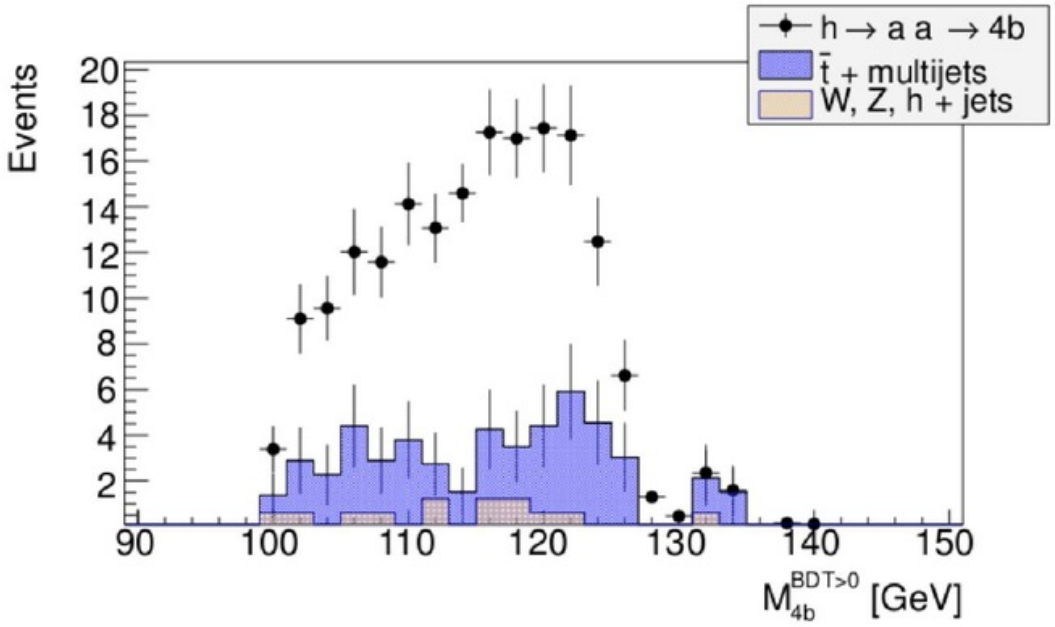

Figure 49: Reconstruted 4b invariant mass distribution for 20 GeV scalar (a) with a BDT cut of > 0.

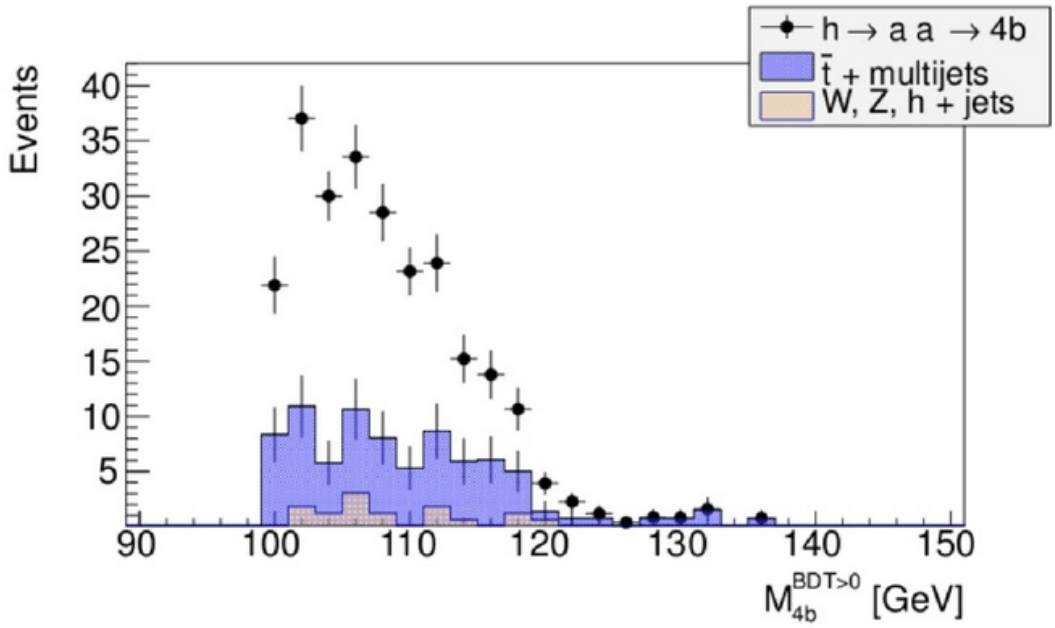

Figure 50: Reconstruted 4b invariant distribution for 60 GeV scalar (a) with a BDT cut of > 0.

The BDT cut of > 0 appears to be an effective cut, with respect to recognising the 4b signal peaks over the background distributions. The observed peaks are somewhat broad however, with

the 60 GeV peak looking shifted towards lower masses, with a less pronounced shoulder near 125 GeV (more of a sloping tail). The 20 and 60 GeV dijet distributions can then be seen in Figures 51 and 52 respectively.

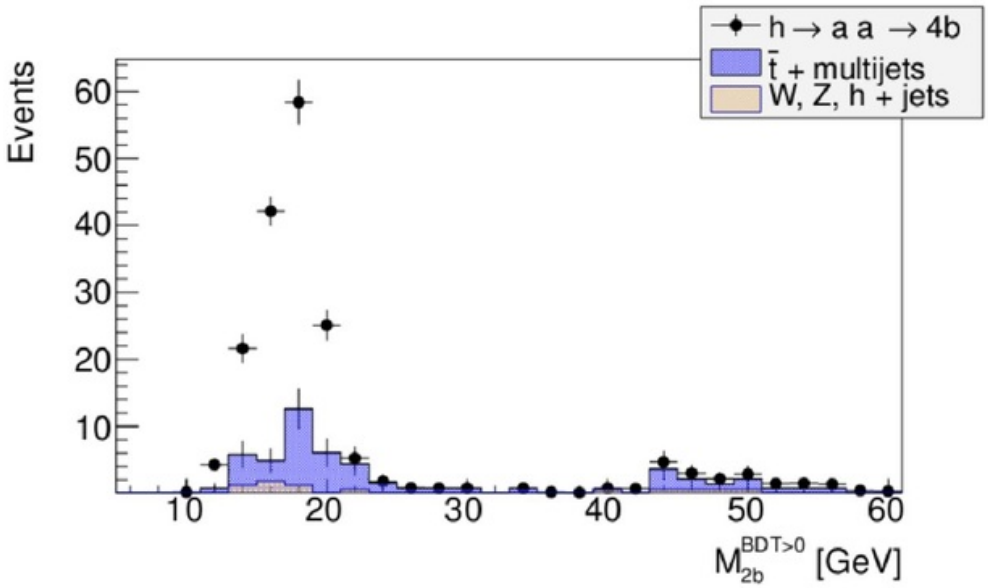

Figure 51: Reconstruted 2b invariant mass distribution for 20 GeV scalar (a) pair 1 with a BDT cut of > 0. See corresponding pair 2 plot in Figure 60 in the Appendix.

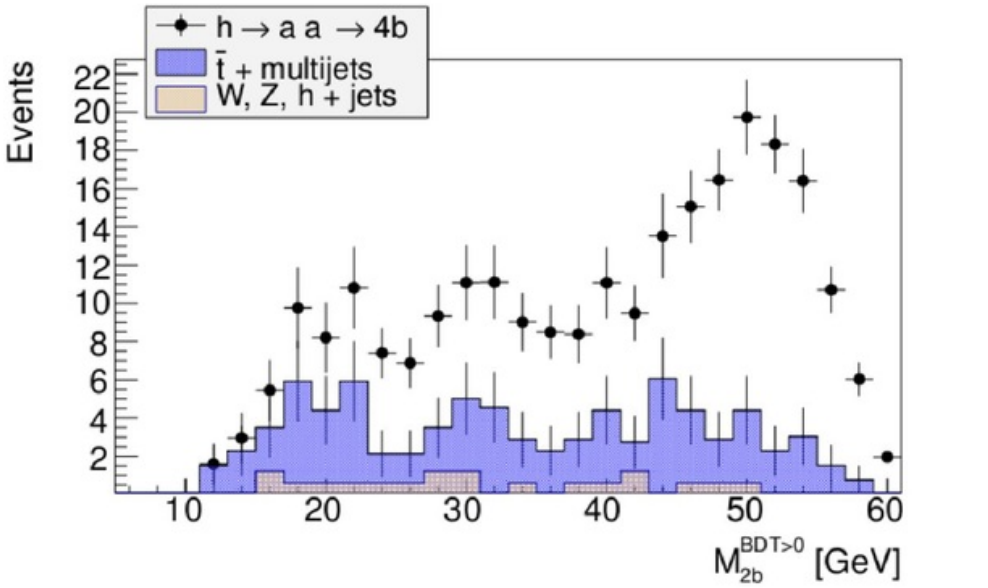

Figure 52: Reconstruted 2b invariant mass distribution for 60 GeV scalar (a) pair 1 with a BDT cut of > 0. See corresponding pair 2 plot in Figure 61 in the Appendix.

Similar to the 4b Higgs peak, the 2b dijet peaks clearly display the 20 and 60 GeV scalar resonances. The same trend as seen in the 4b distribution is again seen in the 2b distribution for the 60 GeV dijet peak, namely a broad resonance width, as compared to the relatively sharp 20 GeV peak.

With the BDT cut of > 0 in place, and an integrated luminosity of 100 fb^{-1} (1 year running at FCChe) and Br($h \to \phi\phi$)=10% and Br($\phi \to b\bar{b}$)=100%, the expected visible cross sections are 1.30 ± 0.13 fb for the 20 GeV scalar and 1.68 ± 0.16 fb for the 60 GeV scalar (Eq. 17 and 18). Compared to the generated cross sections of 52.95 and 52.34 respectively, these visible cross sections represent an acceptance of around 2.5-3% (Eq. 14).

$$\sigma = \frac{N_{sig}}{L} \tag{17}$$

Where N_{sig} is the number of surviving signal events after all cuts and BDT analysis and L is the luminosity.

$$\Delta\sigma = \frac{1}{L \times \sqrt{N_{sig} N_{b1} N_{b2}}} \tag{18}$$

Where N_{b1} and N_{b2} are the number of top+multijet and W/Z/h+multijet background events respectively. These results (obtained with BDT > 0) had significances of 14 and 14.7 respectively, calculated using Eq. 19, which is taken from Eq. 97 of Ref. [45].

$$Z = \sqrt{2\left[(S+B)\ln\left(1+\frac{S}{B}\right) - S\right]} \tag{19}$$

Where S is the number of signal events and B is the number of background events. These significances suggest incredible prospects for measuring this exotic signal process. To investigate further, the significance of different branching scenarios was studied. This helped to gain an estimate of what branchings can obtain the 5σ discovery limit, with a full 10 years running at FCChe (1 ab^{-1} integrated luminosity). Table 9 shows the significances and cross sections for different branching scenarios, with an integrated luminosity of 1 ab^{-1}.

	M_ϕ (GeV)					
	20			60		
BR (%)	σ (fb)	Δσ (fb)	Z	σ (fb)	Δσ (fb)	Z
0.2	0.03	0.02	1.14	0.03	0.03	1.17
0.4	0.05	0.02	2.27	0.07	0.03	2.33
0.6	0.08	0.02	3.37	0.10	0.03	3.47
0.8	0.10	0.02	4.46	0.13	0.03	4.59
1	0.13	0.03	5.54	0.17	0.03	5.71

Table 9: Significances and cross sections for different branching scenarios for M_ϕ= 20 and 60 GeV, at FCChe with an integrated luminosity of 1 ab^{-1} and BDT cut of > 0.

This is assuming the cut flow is the same for different branchings, which may not in fact be the case, and a better result would be obtained by doing the full chain of analysis with the lower branching in from the start. It is seen that a 5σ discovery could be made with a Higgs to ϕ branching of 1%, over the full 10 years running of the FCChe machine.

8 Conclusions

The final visible cross sections obtained, after all cuts, combinatorics and BDT analysis, were 1.30 ± 0.13 fb for the 20 GeV scalar and 1.68 ± 0.16 fb for the 60 GeV scalar, with significances of 14 and 14.9 respectively. These results were obtained for the FCChe collider/detector set up, which has a centre of mass energy of 3.5 TeV, using an integrated luminosity of 100 fb^{-1}, with Br($h \to \phi\phi$)=10% and Br($\phi \to b\bar{b}$)=100% respectively. The 5σ discovery limit was found to be at around Br($h \to \phi\phi$)=1%, with cross sections of 0.13 ± 0.03 and 0.17 ± 0.03 and significances of 5.54 and 5.71 respectively for the 20 and 60 GeV scalars.

Using BDT analysis, the dijet and 4b resonances were clearly discernible, over the dominant CC multijet backgrounds. The other scalar mass candidates, such as the 30 and 40 GeV signals for example, showed promising results in the first estimate of signal to background using the method of dijet mass binning. Extending these studies, in particular also performing BDT analysis for these masses, and adding the dijet mass binning to BDT, could very well also provide strong results and prospects at measurements in these mass ranges.

An outlook for future studies would be to investigate further using a more sophisticated BDT analysis. Different variables could be investigated to gain a more tailored view of the signal and background topologies, and hence an increased efficiency at separating the signal from the background. Also the full analysis chain could be performed for each mass/collider option, extending the scope of the study to detector level for all facility options. To make the study more comprehensive, more backgrounds could be considered, and in particular NC backgrounds as well as $t\bar{t}$ photoproduction, which were qualitatively eliminated in this study, could be investigated. Additionally, different branching scenarios could be investigated through the full analysis chain through to the detector level. This would give a better view at the landscape in which the search is to be performed, gaining insight into what results could be obtained for different branchings without assuming the same cut flow for different branching scenarios. This study provides a benchmark analysis of the decay process and an estimate of the cross sections that one could expect to observe for the process, with very promising results for future analyses.

Bibliography

[1] N. E. Bomark et al. A light NMSSM pseudoscalar Higgs boson at the LHC redux. *JHEP 1502 (2015) 044*, 2014, arXiv:1409.8393.

[2] The ATLAS Collaboration. Observation of a new particle in the search for the Standard Model Higgs boson with the ATLAS detector at the LHC. *Phys. Lett.*, B716:1–29, 2012, 1207.7214.

[3] C. Csaki. The Minimal supersymmetric standard model (MSSM). *Mod. Phys. Lett.*, A11:599, 1996, hep-ph/9606414.

[4] G. Dvali. Black Holes and Large N Species Solution to the Hierarchy Problem. *Fortsch. Phys.*, 58:528–536, 2010, 0706.2050.

[5] S. P. Martin. A Supersymmetry primer. 1997, hep-ph/9709356. [Adv. Ser. Direct. High Energy Phys.18,1(1998)].

[6] B. Delamotte. A Hint of renormalization. *Am. J. Phys.*, 72:170–184, 2004, hep-th/0212049.

[7] K. A. Intriligator and N. Seiberg. Lectures on Supersymmetry Breaking. *Class. Quant. Grav.*, 24:S741–S772, 2007, hep-ph/0702069.

[8] S. Ramos-Sanchez. The mu-problem, the NMSSM and string theory. *Fortsch. Phys.*, 58:748–752, 2010, 1003.1307.

[9] J. Greensite. *An Introduction to the confinement problem.* New York : Springer, 2011.

[10] B.R. Webber. Hadronization: Lectures at Summer School on Hadronic Aspects of Collider Physics, Zuoz, Switzerland, August 1994.

[11] M. Klein. Deep inelastic scattering at the energy frontier. Annalen Phys., 528:138–144, 2016.

[12] Fcc-he: A renaissance of deep inelastic scattering at cern, http://ep-news.web.cern.ch/content/fcc-he-renaissance-deep-inelastic-scattering-cern, 31/04/2014.

[13] LHeC Collaboration. A Large Hadron Electron Collider at CERN: Report on the Physics and Design Concepts for Machine and Detector. 2012, arXiv:1206.2913.

[14] O. Bruning; J. Jowett; M. Klein; D. Pellegrini; D. Schulte; F. Zimmermann. A Baseline for the FCC-he, EDMS 17979910 FCC-ACC-RPT-0012.

[15] M. Klein; U. Klein; P. Kostka. Private Communication, 27 April, 2017.

[16] J. Alwall; R. Frederix; S. Frixione; V. Hirschi; F. Maltoni; O. Mattelaer; H. S. Shao; T. Stelzer; P. Torrielli; M. Zaro. The automated computation of tree-level and next-to-leading order differential cross sections, and their matching to parton shower simulations. *JHEP*, 07:079, 2014, 1405.0301.

[17] A. Alloul; N. D. Christensen; C. Degrande; C. Duhr; B. Fuks. FeynRules 2.0 - A complete toolbox for tree-level phenomenology. *Comput. Phys. Commun.*, 185:2250–2300, 2014, 1310.1921.

[18] T. Sjostrand; S. Mrenna; P. Z. Skands. PYTHIA 6.4 Physics and Manual. *JHEP*, 05:026, 2006, hep-ph/0603175.

[19] A. Giammanco; V. Lemaître; A. Mertens; M. Selvaggi J. de Favereau; C. Delaere; P. Demin. DELPHES 3, A modular framework for fast simulation of a generic collider experiment. *JHEP*, 02:057, 2014, 1307.6346.

[20] R. Brun and F. Rademakers. ROOT - An Object Oriented Data Analysis Framework, Proceedings AIHENP 96 Workshop, Lausanne, Sep. 1996, Nucl. Inst. and Meth. in Phys. Res. A 389 (1997) 81-86. See also (http://root.cern.ch/).

[21] J. Alwall; S. de Visscher; F. Maltoni. QCD radiation in the production of heavy colored particles at the LHC. *JHEP*, 02:017, 2009, 0810.5350.

[22] M. Cacciari; G. P. Salam; G. Soyez. The Anti-k(t) jet clustering algorithm. *JHEP*, 04:063, (2008), 0802.1189.

[23] ATLAS Collaboration. Search for the Higgs boson produced in association with a W boson and decaying to four b-quarks via two spin-zero particles in pp collisions at 13 TeV with the ATLAS detector. *Eur. Phys. J.*, C76(11):605, 2016, 1606.08391.

[24] The CMS Collaboration. Search for exotic decays of the higgs boson to a pair of new light bosons with two muon and two b jets in final states. *CMS PAS HIG-14-041*, 2016.

[25] R. Devenish. Deep Inelastic Scattering. Oxford: Oxford University Press, 2004.

[26] J. Steinberger (2005). Learning about Particles. Springer. p. 130.

[27] J. Pumplin; D. R. Stump; J. Huston; H. L. Lai; P. M. Nadolsky; W. K. Tung. New generation of parton distributions with uncertainties from global QCD analysis. *JHEP*, 07:012, 2002, hep-ph/0201195.

[28] R. D. Ball; V. Bertone; S. Carrazza; L. Del Debbio; S. Forte; A. Guffanti; N. P Hartland; J. Rojo. Parton distributions with QED corrections. *Nucl. Phys.*, B877:290–320, 2013, 1308.0598.

[29] K. Nakamura et al. (PDG), JP G 37, 075021 (2010).

[30] BCDMS Collaboration. A high statistics measurement of the proton structure functions $F_2(x, Q^2)$ and R from deep inelastic muon scattering at high Q^2. *Physics Letters B*, 223(3):485 – 489, 1989.

[31] A. R. Bohm and S. Yoshihiro. Relativistic resonances: Their masses, widths, lifetimes, superposition, and causal evolution. *Phys. Rev.*, D71:085018, 2005, hep-ph/0412106.

[32] V. Barger; M. Ishida; W. Y Keung. Total Width of 125 GeV Higgs Boson. *Phys. Rev. Lett.*, 108:261801, 2012, 1203.3456.

[33] ATLAS Collaboration. Measurements of the Higgs boson production and decay rates and coupling strengths using pp collision data at $\sqrt{s} = 7$ and 8 TeV in the ATLAS experiment. *Eur. Phys. J.*, C76(1):6, 2016, 1507.04548.

[34] A. Denner; S. Heinemeyer; I. Puljak; D. Rebuzzi; M. Spira. Standard Model Higgs-Boson Branching Ratios with Uncertainties. *Eur. Phys. J.*, C71:1753, 2011, 1107.5909.

[35] S. Liu; Y. L. Tang; C. Zhang; S. H. Zhu. Exotic Higgs Decay $h \to \phi\phi \to 4b$ at the LHeC, 2016, arXiv:1608.08458.

[36] LHCb Collaboration. B flavour tagging using charm decays at the LHCb experiment. JINST 10 (2015) P10005.

[37] J. de Favereau de Jeneret and S. Ovyn. Single top quark photoproduction at the LHC. *Nucl. Phys. Proc. Suppl.*, 179-180:277–284, 2008, 0806.4886.

[38] C. W. Fabjan and F. Gianotti. Calorimetry for Particle Physics. 31 October 2003, CERN-EP/2003-075.

[39] A. Hoecker; P. Speckmayer; J. Stelzer; J Therhaag; E. von Toerne; H. Voss. TMVA: Toolkit for Multivariate Data Analysis. *PoS*, ACAT:040, 2007, physics/0703039.

[40] G. McGregor; B. P. Roe; H. J Yang; J. Zhu; Y. Liu; I. Stancu. Boosted decision trees, an alternative to artificial neural networks. *Nucl. Instrum. Meth.*, A543(2-3):577–584, 2005, physics/0408124.

[41] T. Chen and T. He. Higgs Boson Discovery with Boosted Trees. JMLR: Workshop and Conference Proceedings 42:69-80, 2015.

[42] The ATLAS Collaboration. Search for the Standard Model Higgs boson decaying into $b\bar{b}$ produced in association with top quarks decaying hadronically in pp collisions at $\sqrt{s} = 8$ TeV with the ATLAS detector. *JHEP*, 05:160, 2016, 1604.03812.

[43] Y. Freund and R.E. Schapire. A decision-theoretic generalization of on-line learning and an application to Boosting, J. of Computer and System Science 55, 119 (1997).

[44] The CMS Collaboration. Search for New Physics with Jets and Missing Transverse Momentum in *pp* collisions at $\sqrt{s} = 7$ TeV. *JHEP*, 08:155, 2011, 1106.4503.

[45] G. Cowan; K. Cranmer; E. Gros; O. Vitells. Asymptotic formulae for likelihood-based tests of new physics. *Eur. Phys. J.*, C71:1554, 2011, 1007.1727. [Erratum: Eur. Phys. J.C73,2501(2013)].

Appendix

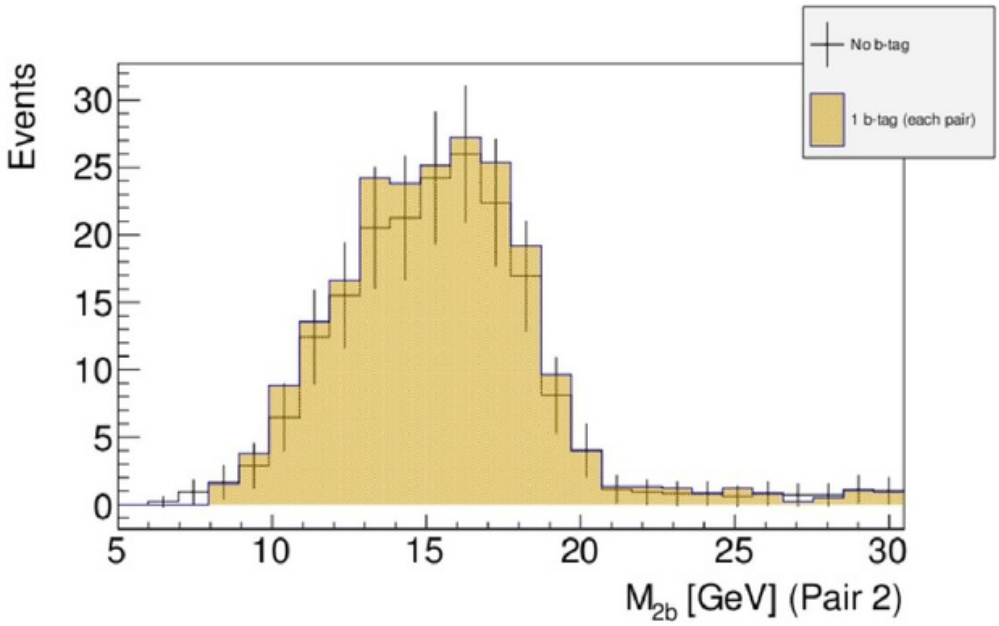

Figure 53: Pair 2 signal plot corresponding to Figure 26.

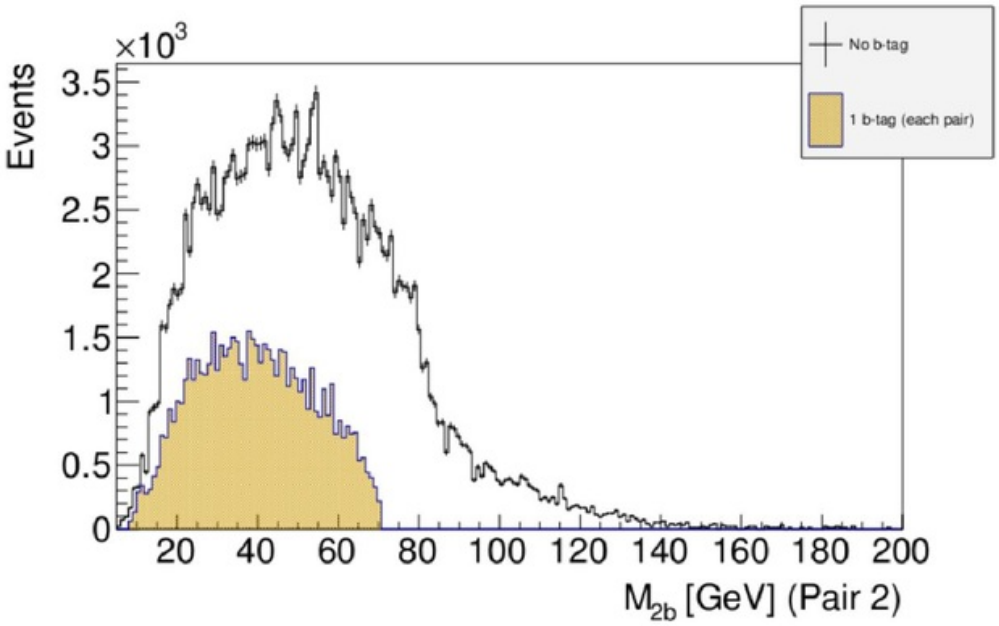

Figure 54: Pair 2 top background plot corresponding to Figure 28.

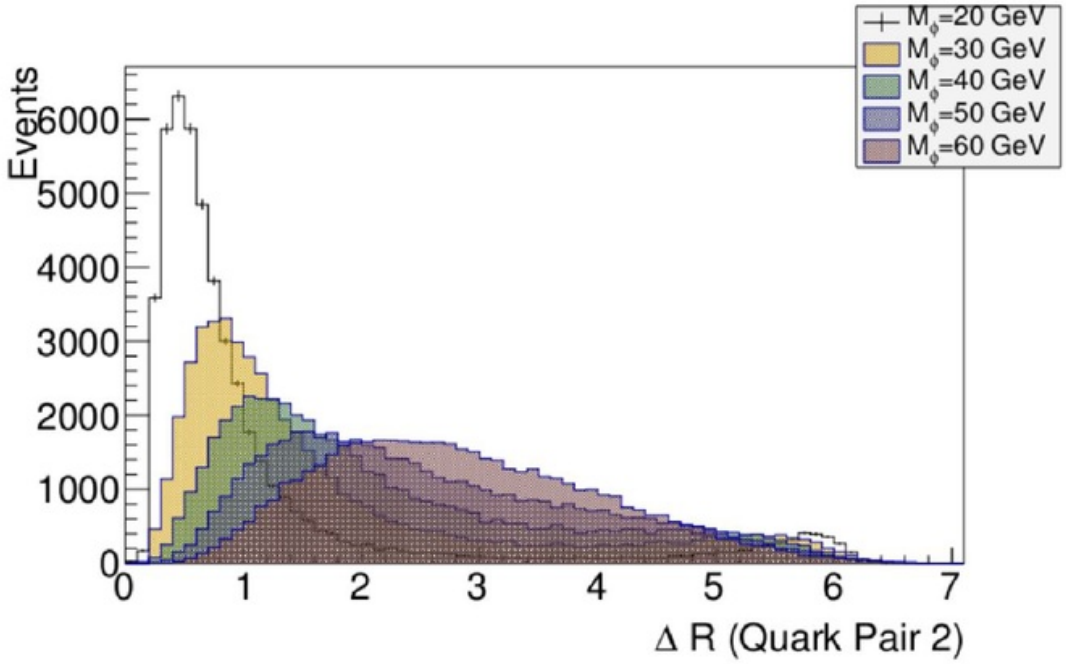

Figure 55: Corresponding dijet distribution to Figure 17.

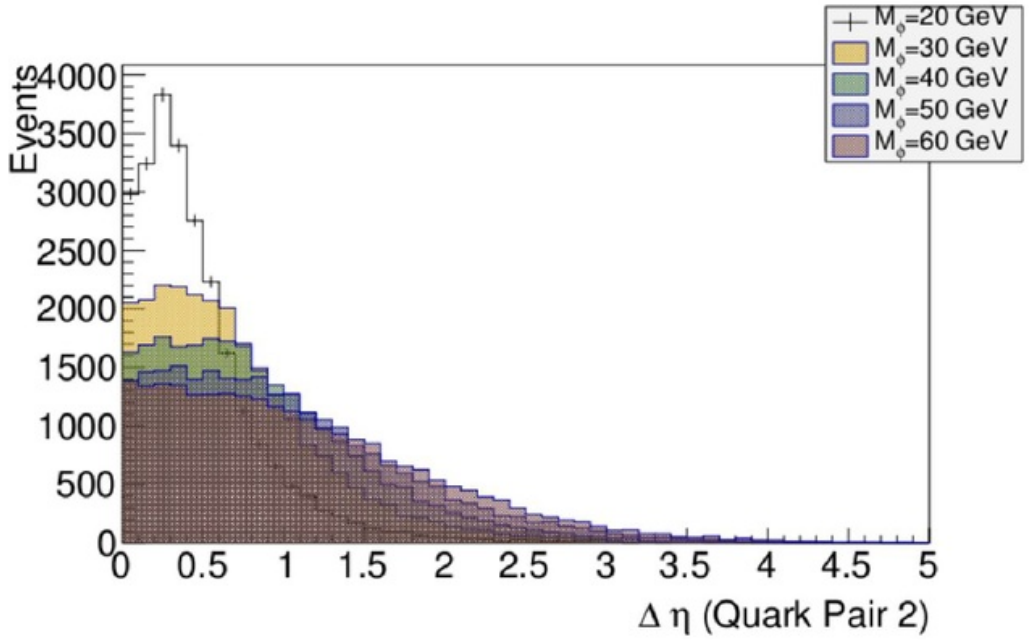

Figure 56: Pair 2 corresponding to Figure 18.

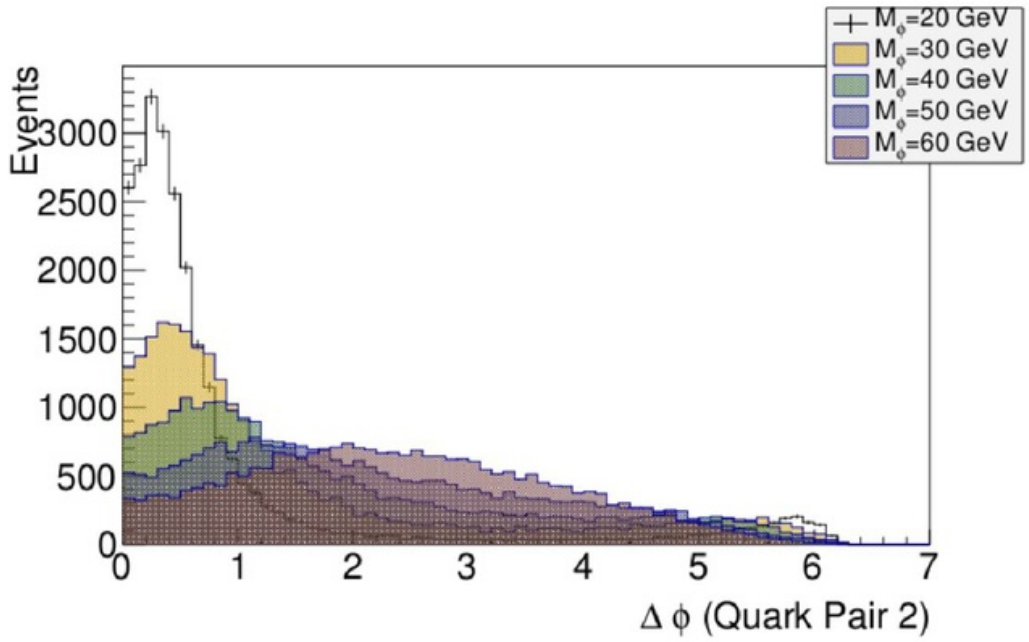

Figure 57: Pair 2 corresponding to Figure 19.

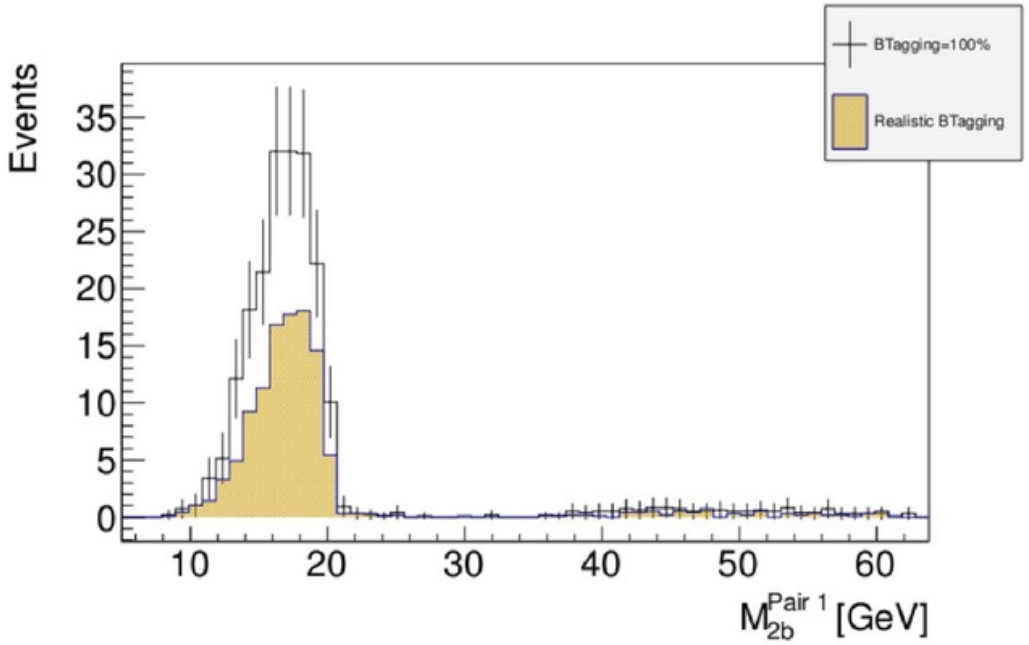

Figure 58: Pair 1 dijet mass peak with both realistic and 100% b-taaging for 20 GeV scalar.

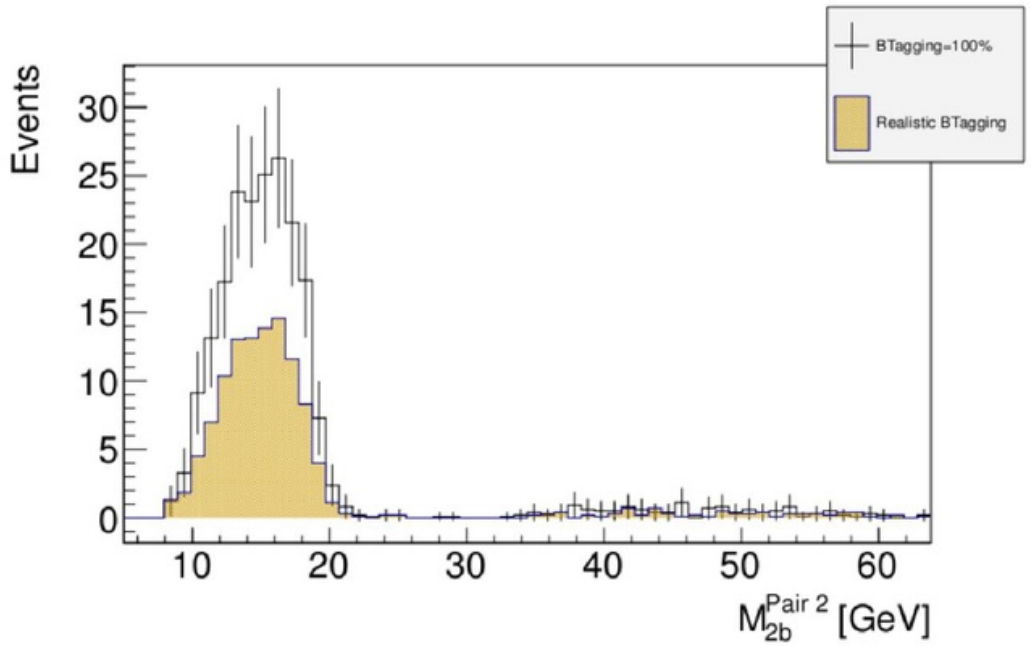

Figure 59: Pair 2 dijet mass peak with both realistic and 100% b-taaging for 20 GeV scalar.

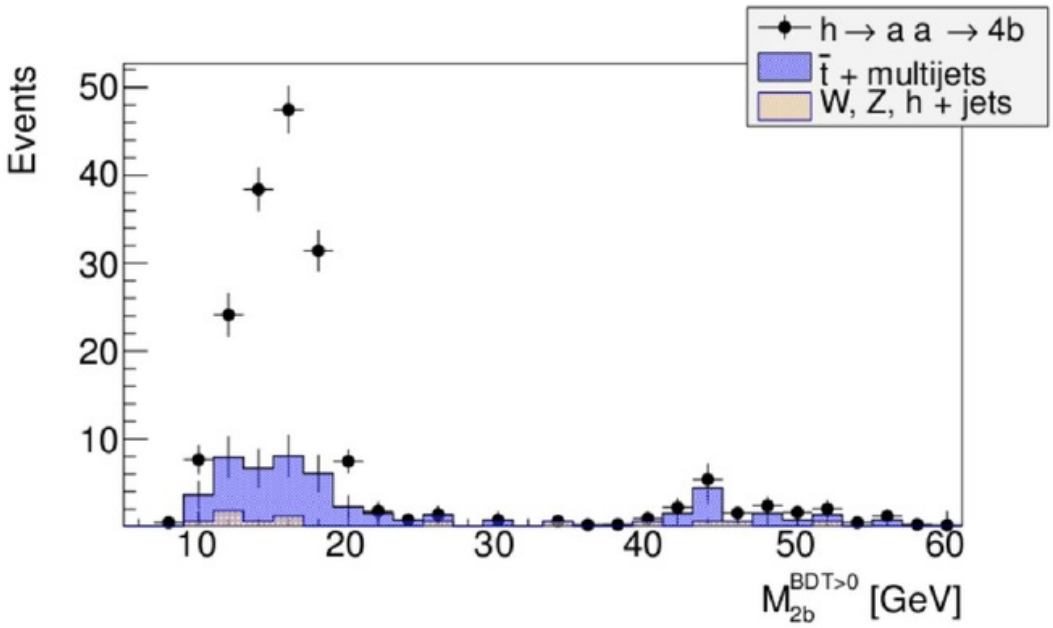

Figure 60: Pair 2 plot corresponding to Figure 51.

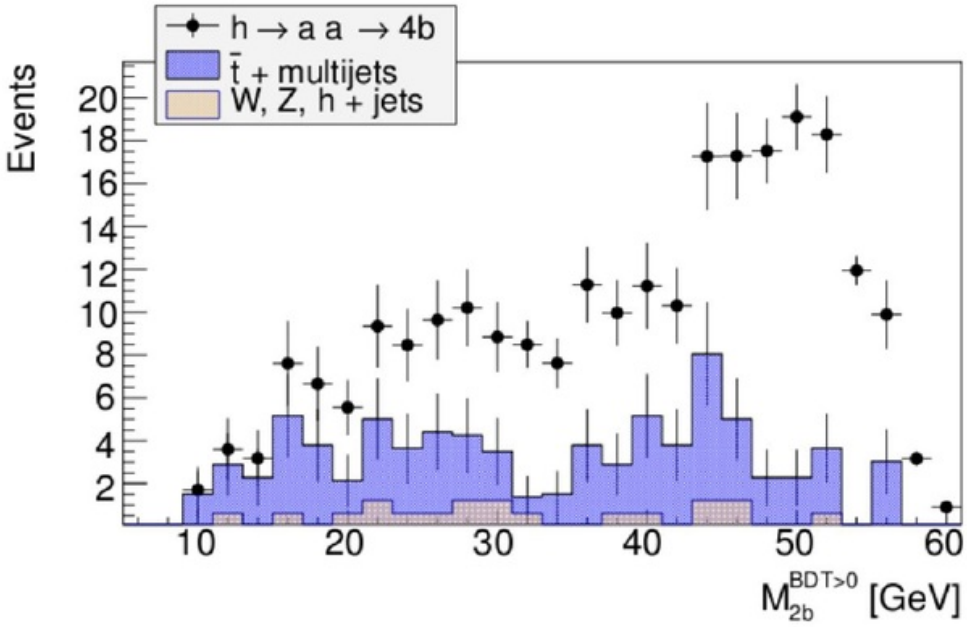

Figure 61: Pair 2 plot corresponding to Figure 52.

Study of Exotic Higgs Decay at Electron-Hadron Colliders

GRADEMARK REPORT

FINAL GRADE

/0

GENERAL COMMENTS

Instructor

PAGE 1

PAGE 2

PAGE 3

PAGE 4

PAGE 5

PAGE 6

PAGE 7

PAGE 8

PAGE 9

PAGE 10

PAGE 11

PAGE 12

PAGE 13

PAGE 14

PAGE 15

PAGE 16

PAGE 17

PAGE 18

PAGE 19

PAGE 20

PAGE 21

PAGE 22

PAGE 23

PAGE 24

PAGE 25

PAGE 26

PAGE 27

PAGE 28

PAGE 29

PAGE 30

PAGE 31

PAGE 32

PAGE 33

PAGE 34

PAGE 35

PAGE 36

PAGE 37

PAGE 38

PAGE 39

PAGE 40

PAGE 41

PAGE 42

PAGE 43

PAGE 44

PAGE 45

PAGE 46

PAGE 47

PAGE 48

PAGE 49

PAGE 50

PAGE 51

PAGE 52

PAGE 53

PAGE 54

PAGE 55

PAGE 56

PAGE 57

PAGE 58

PAGE 59

PAGE 60

PAGE 61

PAGE 62

PAGE 63

PAGE 64

PAGE 65

PAGE 66

PAGE 67

PAGE 68

PAGE 69

PAGE 70